



HAL
open science

Plasticity and ductility of an anisotropic recrystallized AA2198 Al-Cu-Li alloy in T3 and T8 conditions during proportional and non-proportional loading paths: simulations and experiments

Xiang Kong, Jianqiang Chen, Yazid Madi, Djamel Missoum-Benziane, Jacques Besson, Thilo F. Morgeneyer

► To cite this version:

Xiang Kong, Jianqiang Chen, Yazid Madi, Djamel Missoum-Benziane, Jacques Besson, et al.. Plasticity and ductility of an anisotropic recrystallized AA2198 Al-Cu-Li alloy in T3 and T8 conditions during proportional and non-proportional loading paths: simulations and experiments. 2021. hal-03497233v1

HAL Id: hal-03497233

<https://hal.science/hal-03497233v1>

Preprint submitted on 20 Dec 2021 (v1), last revised 15 Mar 2023 (v3)

HAL is a multi-disciplinary open access archive for the deposit and dissemination of scientific research documents, whether they are published or not. The documents may come from teaching and research institutions in France or abroad, or from public or private research centers.

L'archive ouverte pluridisciplinaire **HAL**, est destinée au dépôt et à la diffusion de documents scientifiques de niveau recherche, publiés ou non, émanant des établissements d'enseignement et de recherche français ou étrangers, des laboratoires publics ou privés.



Distributed under a Creative Commons Attribution 4.0 International License

Plasticity and ductility of an anisotropic recrystallized AA2198 Al-Cu-Li alloy in T₃ and T₈ conditions during proportional and non-proportional loading paths: simulations and experiments

X. Kong¹, J.Q. Chen^{1,2}, Y. Madi¹, D. Missoum-Benziane¹, J. Besson¹, and T.F. Morgeneyer¹

¹ MINES ParisTech, PSL University, Centre des Matériaux, CNRS UMR 7633, Evry, France

² Pratt Whitney Canada, 1000 Boul. Marie-Victorin, Longueuil, QC J4G 1A1 Canada

The anisotropic material behaviour of a recrystallized AA2198 Al-Cu-Li alloy in T₃ and T₈ conditions was assessed by proportional loading of uniaxial-tension specimens in rolling (L), transverse (T) and diagonal (D) orientations. The width and longitudinal strains were measured to quantify plastic anisotropy. Notched-tension samples were tested in L and T directions. The material showed weak anisotropy in terms of stress strain curves and a moderate plastic anisotropy, consistent with its texture obtained by EBSD. An anisotropic Bron-Besson type material model was identified using this data base and a micro shear-only (SO) test. The model succeeded in predicting the behaviour of micro specimens for proportional tension-only (TO) loading and non-proportional load path changes including ‘shear to tension’ (ST) as well as ‘tension to shear’ (TS) tests. The non-proportional loading was achieved using a newly designed cross shaped sample. It was loaded in one direction, unloaded and subsequently loaded in the orthogonal direction till fracture. The average stretch to fracture of both alloys measured by a four point frame optical extensometer decreased by 29% and 16% for T₃ and T₈ respectively for the ‘shear to tension’ experiment compared to the proportional TO experiment. This reduction was suspected to be linked to either damage development under shear and/or high stress levels during tension due to the hardening of the material during shear. The average stretch to fracture of ‘tension to shear’ tests was reduced by 10% for 2198T₃ and hardly reduced for 2198T₈ compared to the stretch to fracture of the SO tests. However, the results exhibited a strong scatter for both heat treatments. The ductility scatter was attributed to necking and damage development in tension that can affect strain localization, associated fracture path and ductility, as observed by DIC and fractography.

Keywords Al-Cu-Li alloy, plastic anisotropy, characterization, non-proportional load path change, ductile fracture

1 Introduction

Aluminium alloys have been widely used and their performance has been improved to meet the demands in aerospace industry for a long time (Ehrström et al. 2000, Warner 2006). The latest Al-Cu-Li alloys are increasingly used for their high specific strength and excellent damage tolerance. The third generation of Al-Cu-Li alloys (i.e. 2198, 2098 and 2050) have successfully balanced the toughness and strength after optimizing the Cu/Li ratio. While partly sacrificing the advantage of Li addition, which is the increase in modulus and the decrease in density, it led to an increase in strength potential and thermal stability (Warner 2006). Among this third generation, 2198 Al-Cu-Li alloy exhibits a good combination of static tensile properties, damage tolerance, formability and good properties after friction stir welding (Chen 2011; Le-Jolu et al. 2010). AA2198 in various heat treatment conditions has been studied in (Deschamps et al. 2013; Nayan et al. 2019) and an anisotropic plastic behaviour has been found (Chen 2011; Nayan et al. 2019). This anisotropy is particularly strong for the fibrous material (Chen et al. 2011).

Ductile fracture at high stress triaxiality (i.e. above 1) has been widely studied over the last decades and the governing damage mechanisms have been identified as void nucleation-growth-coalescence (Pineau et al. 2016). More recent studies have focused on the fracture at low stress triaxiality and complex relationships between strain to fracture and stress triaxiality have been found by Bao et al. 2004. Phenomenological models have been applied and attempted to fit the experimental behaviour in terms of strain, stress triaxiality and the Lode parameter (Bao et al. 2004). However, strain to fracture is an ambiguous definition and difficult to measure especially in regions where strains are highly localized, not to mention the strain definition during complex non-proportional load path changes.

Mechanisms under proportional loading at low stress triaxiality are not as clear as at high stress triaxiality yet. Gross et al. 2016 performed a shear experiment via *in situ* scanning electron microscope on a sheet specimen of Aluminum alloy 6061-T6. Second phase particles on the free surface were seen to break, debond or rotate and pre-existent voids were suspected to have a minimal influence on the deformation of this material under shear. No severe damage and/or failure were found on the surface region of nearly zero triaxiality even the local strain reached up to 1.

With the aim of studying the damage evolution inside the bulk of the material during complex load path changes, advanced techniques as three-dimensional (3D) synchrotron imaging are necessary to perform *in situ* experiments. 3D synchrotron laminography is suited to image the regions of interest in flat samples (Helfen et al. 2012). In order to achieve high resolution observation, samples need to be miniaturized with dimensions of the regions of interest in the order of 1 mm³. Roth et al. 2018b investigated the interior damage mechanism of a ‘smiley’ shear specimen via *in situ* laminography of a dual phase steel. Tancogne-Dejean et al. 2021 analysed the same specimen geometry for a 2024 alloy with the same technique. They both observed the void nucleation on intermetallic particles, rotation and growth. The debonding or failure of the brittle particles was normal to maximum principal stress direction.

Concerning small samples, there is a doubt if the limited grain number in miniaturized sample is still able to guarantee the homogeneous mechanical fields and good repeatability of the macroscopic sample behavior. Gorji et al. 2021 performed different uniaxial tension, notched tension, central hole and in plane shear tests on a steel alloy for both 2 mm thick macro-samples and the miniaturized 0.1 mm thickness micro-samples. They found that the plasticity obtained from micro-samples matched the one from conventional macro-samples but failure strain slightly reduced in the miniaturized samples due to the deleterious effect of surface roughness that is substantial for the micro-samples.

Most engineering structures, especially thin sheet, usually undergo load path changes during manufacturing and/or forming followed by in service loading. Xavier et al. 2015 found that non-proportional strain paths of an interstitial steel sheet showed significantly smaller limit strains than the proportional path based on the values from the forming limit curve. The macroscopic effect of pre-load has been investigated for some complex load path change experiments. In order to achieve load path change experiments, some research groups conducted the pre-straining of the raw sheet and then the specimens were cut from the deformed sheet as virgin ones before turning to the second loading (Tarigopula et al. 2009; Abedini et al. 2018; Madi et al. 2020). Tarigopula et al. 2009 conducted the uniaxial tension pre-strainings to 1%, 4% and 8% on raw sheet of dual phase steel and shear specimens were machined from the deformed region then they were tested till fracture. At the macroscale, the deformation at fracture under shear only decreased for the 8% pre-strained samples: the macroscopic strain to fracture was reduced by about 30% compared to the tests without pre-loading. The effects of the 2%, 4% to 6% pre-strainings were studied using tensile bars for a high-strength steel (Madi et al. 2020). They found a decrease in both ductility and toughness with increasing prestrains. The ductility can decrease pronouncedly even with only 2% pre-straining. Abedini et al. 2018 performed shear tests after uniaxial and bi-axial preloadings using a Mg alloy ZEK100 and they found that the global displacement at fracture for both prestrain conditions decreased by around 20% compared to proportional shear tests. Other groups designed special geometries for the load path change (Papasidero et al. 2015; Gerke et al. 2019; Brünig et al. 2021). Papasidero et al. 2015 applied torsion-tension test on an axisymmetric tube specimen of AA2024 T351. Macroscopically, the global displacement to fracture of tension tests conducted after pre-torsion was reduced by 10% compared to the proportional tension test. Remarkably, the global rotation to fracture in torsion tests conducted after pre-tension loading decreased nearly by 30% compared to the proportional torsion test. Gerke et al. 2019 designed a suitable cruciform X₀-specimen on Aluminum alloy 6082 T6. The different stress states and load paths were achieved by controlling the ratio of bi-axial displacements. Brünig et al. 2021 investigated the complex shear and tension load path changes using an H shaped geometry made of the same 6082 T6 Aluminum alloy. Non-proportional loadings including different extents of shear pre-straining followed by tension and different tension pre-strainings followed by shear were conducted. A remarkable displacement reduction was found due to pre-straining. The higher the pre-strain was, the higher the reduction in ductility. However, the knowledge on damage mechanism under non-proportional load path change was not clearly identified by only observing fracture surfaces.

The present work has several objectives:

- To characterize the plastic behavior including the plastic anisotropy of the material in two different heat treatment conditions.
- To design a suitable miniaturized sample geometry for a ‘shear to tension’ or ‘tension to shear’ load path change in an *in situ* imaging environment for another study (Kong et al. 2021).
- To study the effect of sample miniaturization on test repeatability.
- To identify the effect of a load path change on ductility.
- To fit a macroscopic anisotropic plasticity model using proportional loading tests and assess its predictive capabilities for non-proportional loading and associated mechanical fields under these conditions.

In this paper, the material microstructure is characterized first in terms of grain size and texture, as well as particle and void content. The strain measurement using an optical extensometer is detailed. The anisotropic material model is shortly recalled and the parameter identification procedure explained. In terms of mechanical test results, the microhardness profile through the sample thickness are given and stress strain curves for different loading directions of smooth and notched samples are then gathered for the two heat treatment conditions. The results of repeated testing of small samples for proportional

shear loading or tension loading are shown. They are then compared to ‘shear to tension’ or ‘tension to shear’ load path change results. The non-proportional tests use a specially designed cross shaped sample. Strain fields before fracture obtained by DIC and FE simulations as well as fractography are given. In the modelling part of the paper, the anisotropic plasticity model is first identified using the database of the smooth and notched tensile samples and the small shear sample. The identified model is used to predict the stress-stretch responses for the non-proportional loading paths. The results are subsequently discussed.

2 Materials and methods

2.1 Materials and microstructures

AA2198 was developed by Constellium. The alloy has a slightly lower copper content compared to AA2098 and also has some other minor chemistry adaptations (Ag, Zr ...) to optimize toughness. Table.1 gives the chemical composition limits for AA2198 alloy. In this work, two different tempers of recrystallized AA2198 aluminum-copper-lithium alloy sheets with a nominal thickness of 2 mm were supplied by Constellium. The two different heat treatment conditions (T351 for naturally aged and T851 for artificially aged) are studied. They are referred to as ‘R’ (recrystallized materials). The alloys are obtained by cold rolling followed by industrial finishing treatment: solution heat treatment, water quench, stretch and either naturally aging (T351 condition), or artificial aging to obtain T851 temper. The materials will be referred to as 2198T3R and 2198T8R. In the following, the rolling direction is noted as L, the long transverse direction as T and short transverse direction (thickness direction) as S. D stands for the diagonal direction (45° between L and T in the sheet plane).

	Cu	Li	Zn	Mn	Mg	Zr	Si	Ag	Fe
wt. %	2.9-3.5	0.8-1.1	≤0.35	≤ 0.5	0.25-0.8	0.04-0.18	≤ 0.08	0.1-0.5	≤ 0.01

Table 1: Nominal chemical composition limits of 2198 alloy (wt %).

Micrographs of grain structure were obtained from electron back-scatter diffraction (EBSD) analysis in a FEI Nova nanosem 450FEG with the EDAX-TSL Hikari camera using a step size of 0.5 micrometer and an acceleration voltage of 15 kV. A representative grain structure for 2198T8R is shown in Fig.1 (a). Large pancake shaped grains can be found in the L-T plane. The grain size was measured by using a mean linear intercept method on EBSD data as 82 μm in L, 80 μm in T and 20 μm in S directions. A moderate texture is found in the inverse pole figure Fig.1 (b). This moderate texture is consistent with the moderate anisotropic plasticity for this material as will be seen in the following. 2D sections from Synchrotron Radiation Computed Laminography (SRCL, Helfen et al. 2005), which was performed at European Synchrotron Radiation Facility (ESRF) ID19, for the undeformed material 2198T8R is shown in Fig.1 (c) where the matrix appears in grey and intermetallic particles in white. The voxel size was 0.72 μm. The mean intermetallics content is 0.34% and the initial porosity is very limited (less than 0.04%) compared to other aerospace aluminium alloys (Morgenyey et al. 2009; Tancogne-Dejean et al. 2021).

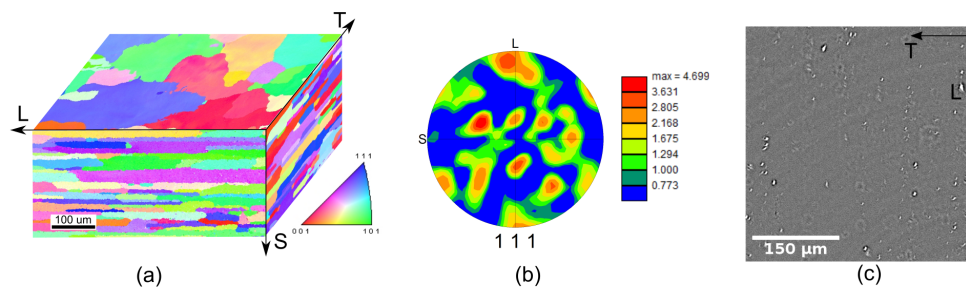


Figure 1: (a) Inverse pole figure indicating the 3D grain structure of 2198T8R sheet material via EBSD (the crystal orientations are given with respect to the normal of each plane), (b) Pole figure of 2198T8R and (c) 2D section of 2198T8R from high resolution 3D X-ray laminography in the L-T plane.

2.2 Mechanical testing

A series of experiments was performed to characterize the mechanical behavior of both alloys (2198T3R and 2198T8R). Specimens were designed for different stress states varying from low triaxiality to more elevated levels of triaxiality and from proportional to non-proportional loadings.

2.2.1 Specimen geometries: macro and micro specimens

All specimens were manufactured from 2 mm thick raw sheet by the means of electrical discharge machining (EDM). Macro specimens of 2 mm thickness including (a) uniaxial-tension (UT), (b) notched-

tension samples (NT₂) with a notch of 2 mm radius were designed for proportional loadings at elevated triaxiality in Fig. 2. The UT samples were loaded in L, T and D directions and the NT sample in L and T direction. A series of 1 mm thick micro specimens were tested to generate a shear state shear inspired by Roth et al. 2018a including (c) shear-only (SO) loaded in L direction, (d) tension-only (TO) loaded in T direction and (e) cruciform sample geometry were especially designed for non-proportional loadings: ‘shear to tension’ (ST) or ‘tension to shear’ (TS), see table 2. The original geometry was miniaturized to be able to image the region of interest at micrometric spatial resolution by 3D synchrotron laminography imaging (Morgeneyer et al. 2021). The vertical and horizontal offset of the region between both notches in Fig. 2 (f) have been calculated and optimized by finite element simulations. The offset is necessary to keep the triaxiality levels around the notches small and to let the sample fail from the shear zone. The idea of the present work is to load the sample also in the direction normal to the shear ligament to achieve a load path change. It should be noted that due to the shift of the notches the tensile loading state may be slightly different to the one obtained by classical notched tensile samples with aligned notches: Some local shear loading may be induced during tension due the offset of the notches. This will be measured in any case by the four point extensometer as explained in the following.

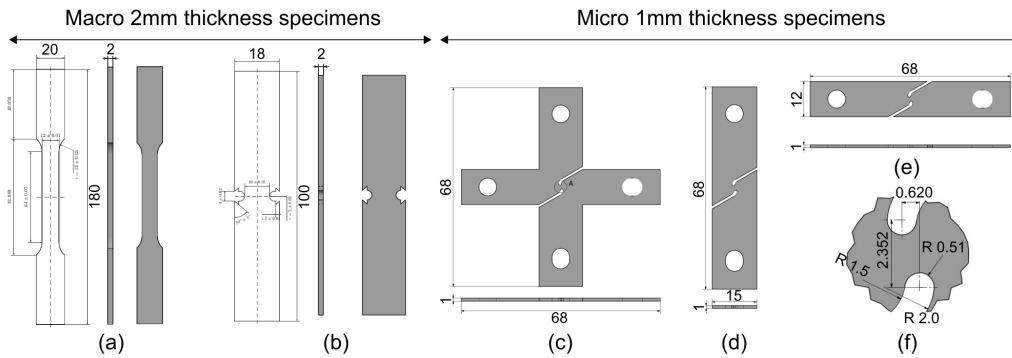


Figure 2: Macro specimen geometries with 2 mm thickness: (a) Uniaxial-tension (UT), (b) Notched-tension (NT₂) and micro specimen geometries with 1 mm thickness: (c) Shear-tension cruciform for non-proportional loadings, (d) Shear-only (SO), (e) Tension-only (TO) samples and (f) the detailed geometry of the region of interest (ROI).

2.2.2 Loading machine setup

All mechanical tests were carried out at room temperature. Macro tension tests (UT and NT₂) were conducted on a servo-hydraulic testing machine. Classical extensometers were used to measure gauge length change both in longitudinal and width directions for UT at strain rate of $10^{-4} s^{-1}$. Notch opening displacements on both the left and the right side were measured for NT₂ specimens and the cross head velocity was set as 200 $\mu m/min$. Micro specimen tests including proportional loadings (SO, TO) and non-proportional loadings (ST, TS) were performed on a dedicated electromechanical loading device for *in situ* laminography testing with 5 kN load cell (ME-Meßsysteme KD40s, Morgeneyer et al. 2021) where cross heads pulled or unloaded at a speed of 5 $\mu m/s$ during both loading and unloading, see table 2.

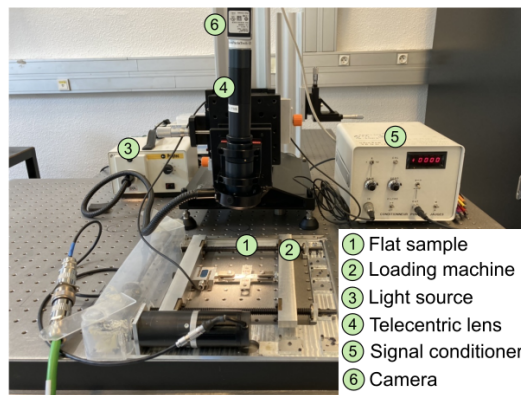


Figure 3: Experimental set up: ① Flat sample on ② Loading machine. Optics: ⑥ camera ④ telecentric lens and ③ light source. The signal of load cell is connected to ⑤ signal conditioner.

2.2.3 Optics setup for strain measurement for micro specimens

In order to measure deformation in the region of interest (ROI) of the complex micro specimens and to avoid being influenced by machine elastic deformation, an optical setup was used to measure the

Specimen	cross head velocity ($\mu\text{m}/\text{min}$)	loading directions
Uniaxial-tension (UT)	384	L, T and D
Notched-tension (NT2)	200	L and T
Shear-only (SO)	300	L
Tensino-only (TO)	300	T
Cross sample	300	shear in L, tension in T

Table 2: Macro and micro specimen loading conditions.

deformation in the region of interest by an optical flow technique (digital image correlation, DIC). In addition, the measurement was used to compare the experiments with finite element simulations. A fine random speckle pattern was deposited by airbrush on the micro specimen surface to measure the displacement fields. The average speckle size was about $15 \mu\text{m}$ and can be seen in Fig.4 (a). Surface images were continuously captured at a frequency of 2 Hz. The detector size is 2048×2048 pixels (Basler acA2040 25g) with optic lens (SILL TZM 0420/3.0-C telecentric lens) resulting in a physical pixel size around $1.87 \times 1.87 \mu\text{m}^2$. Based on the commercial software *vic2D - 6* (Correlated Solutions), the displacement field was measured with subset size set as 55 pixels ($102 \mu\text{m}$) and step size as 5 pixels ($9 \mu\text{m}$). The Hencky strain field was obtained with filter size of 15.

Macro measurement Instead of utilising the local displacement of two points as traditional extensometer for uniaxial tensile experiments, a 4-point-frame optical extensometer, shown in Fig.4 was introduced to measure tension stretch in both vertical and horizontal directions as well as the shear angle in the ROI and to obtain an average macro measurement in the reference frame. The same 4-point-frame measurement was applied in numerical simulations to compare to experiments.

The relative displacement was obtained from the correlation results of optical images at each step. The displacement field was generated using bi-linear interpolation functions corresponding to the 4 selected material points. The region of interest is mainly under simple shear state, according to the specific geometry, when vertical shear load is applied. The deformation gradient F_{ij} is the derivative of the deformed configuration position vector x_i with respect to the reference configuration position vector X_j (Belytschko et al. 2000). In order to remove the rigid body rotation term, \mathbf{R} can be written by polar decomposition as the product of two tensors: a rotation tensor \mathbf{R} and a symmetric right stretch tensor \mathbf{U} .

$$F_{ij} = \frac{\partial x_i}{\partial X_j} = R_{ik} \cdot U_{kj} \quad (1)$$

Tension stretch U_{11} and the absolute value of shear stretch U_{12} were chosen as the tension and shear local measurements respectively.

$$\mathbf{U} = \begin{bmatrix} U_{11} & U_{12} \\ U_{12} & U_{22} \end{bmatrix} \quad (2)$$

Accumulated equivalent strain measurement Damage is accumulated during the complex non-proportional loading path. It is thus important to define an accumulated strain to estimate the strain to fracture under complex loading paths. The logarithmic strain (Hencky strain or true strain) provides the correct measurement of the final strain when deformation takes place in a series of increments, taking into account the influence of the strain path and is defined as:

$$\boldsymbol{\varepsilon} = \frac{1}{2} \log(\mathbf{F}^T \cdot \mathbf{F}) \quad (3)$$

Onaka (Onaka 2010; Onaka 2012) confirmed that the measure is appropriate especially for large simple shear strain.

During the load path change, the equivalent strain needs to be cumulative to estimate an effective strain. The work-conjugate equivalent strain was defined in terms of the adopted constitutive model (Abedini et al. 2018). Butcher et al. 2017 pointed out that the difference between the work-conjugate strain and the accumulated equivalent strain is negligible when strain is less than 0.8. The present work aims to compare the experimental results from DIC with the FEA ones and offer an appropriate measure during complex load path change. The equivalent strain is defined as:

$$\varepsilon_{cum} = \int \sqrt{\frac{2}{3} d\boldsymbol{\varepsilon} : d\boldsymbol{\varepsilon}} \quad (4)$$

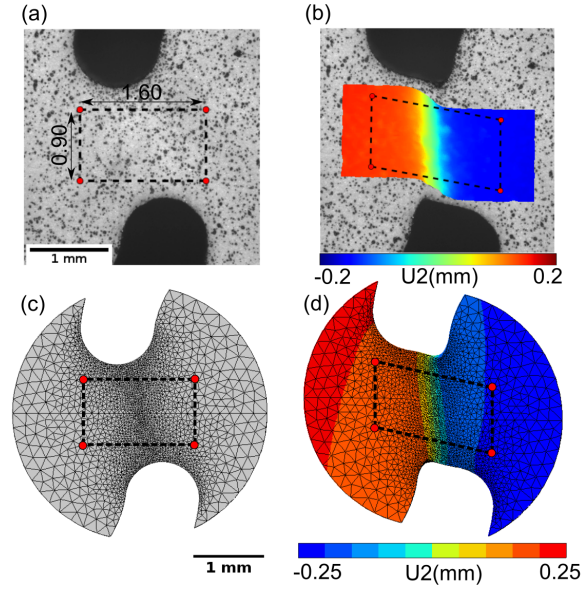


Figure 4: 4-point-frame optical extensometer on (a) reference and (b) deformed images for image correlation and the same 4-point-frame is chosen in (c) initial and (d) deformed steps from finite element model to compare experiment with the simulation. The shown displacement field was calculated by VIC2D locally.

However, the information in thickness direction lacks in the 2D image correlation. The third component ϵ_{III} is computed assuming plastic incompressibility $\epsilon_I + \epsilon_{II} + \epsilon_{III} = 0$, where ϵ_I , ϵ_{II} , ϵ_{III} are the eigenstrains. Hence, the accumulated equivalent strain increment is calculated as:

$$\Delta \epsilon_{cum}^{2d} = \sqrt{\frac{2}{3}(\Delta \epsilon_I^2 + \Delta \epsilon_{II}^2 + \Delta \epsilon_{III}^2)} = \frac{2}{\sqrt{3}} \sqrt{\Delta \epsilon_I^2 + \Delta \epsilon_{II}^2 + \Delta \epsilon_I \Delta \epsilon_{II}} \quad (5)$$

2.3 Numerical simulation

The finite element method was applied to fit an anisotropic plasticity model and predict the stress response under different non-proportional load paths. The macro UT samples were meshed as single element of the quadratic hexahedral element (c3d8). Due to geometry symmetry, an eighth of macro NT2 sample was meshed, while half thickness of the micro sample series was meshed. Micro specimens were meshed using tetrahedra elements (10 nodes, 4 Gauss points), whereas macro specimens were meshed with hexahedral elements (20 nodes and 8 Gauss points). For computation efficiency in model calibration, the coarse mesh size is 200 μm . After the model was optimized, the fine mesh size varied from 30 μm to 100 μm illustrated in Fig. 4 (c)(d). For brevity, the mesh convergence study on stretch-stress from 200 μm down to 10 μm is shown in Appendices A.1. A mixed displacement-pressure updated Lagrangian formulation was applied for the tetrahedral element (c3d10) to account for large plastic strain and incompressibility especially for the micro specimen series (Al Akhrass et al. 2014; Taylor 2000). All simulations are performed in the finite element software Z-set (Besson et al. 1997).

2.3.1 Anisotropic model

The material under study presents an anisotropic plastic behaviour that cannot be represented by a simple quadratic yield surface such as the one proposed in Hill 1950 as this model is unable to satisfactorily describe yield anisotropy and Lankford coefficients simultaneously in all directions. To overcome this difficulty, the yield function proposed by Bron et al. 2004 was used in this work. This phenomenological yield function was developed to represent the plastic anisotropy of the aluminium alloy. It is an extension of the functions given in Barlat et al. 1991; Karafillis et al. 1993. Plastic anisotropy is represented by 12 parameters in the form of two fourth order symmetric tensors. Four other parameters influence the shape of the yield surface uniformly. The model is based on the definition of an equivalent stress $\bar{\sigma}$ function of the stress tensor σ :

$$\bar{\sigma} = (\alpha_1 \bar{\sigma}_1^a + \alpha_2 \bar{\sigma}_2^a)^{1/a} \quad (6)$$

with $\alpha_2 = 1 - \alpha_1$. $\bar{\sigma}_1$ and $\bar{\sigma}_2$ are respectively given by:

$$\bar{\sigma}_1 = \left(\frac{1}{2} (|S_1^2 - S_1^3|^a + |S_1^3 - S_1^1|^a + |S_1^1 - S_1^2|^a) \right)^{1/a} \quad (7)$$

$$\bar{\sigma}_2 = \left(\frac{3^a}{2^a + 2} (|S_2^1|^a + |S_2^2|^a + |S_2^3|^a) \right)^{1/a} \quad (8)$$

where S_1^1, S_1^2, S_1^3 (resp. S_2^1, S_2^2, S_2^3) are the eigenvalues of a modified stress deviator \mathbf{s}_1 (resp. \mathbf{s}_2) defined as: $\mathbf{s}_1 = \mathbf{L}_1 : \boldsymbol{\sigma}$ (resp. $\mathbf{s}_2 = \mathbf{L}_2 : \boldsymbol{\sigma}$) where the fourth order $\mathbf{L}_{1,2}$ have the following form using Voigt notation:

$$\mathbf{L}_k = \begin{pmatrix} (c_k^{LL} + c_k^{SS})/3 & -c_k^{SS}/3 & -c_k^{LL}/3 & 0 & 0 & 0 \\ -c_k^{SS}/3 & (c_k^{SS} + c_k^{TT})/3 & -c_k^{TT}/3 & 0 & 0 & 0 \\ -c_k^{LL}/3 & -c_k^{TT}/3 & (c_k^{TT} + c_k^{LL})/3 & 0 & 0 & 0 \\ 0 & 0 & 0 & c_k^{TL} & 0 & 0 \\ 0 & 0 & 0 & 0 & c_k^{LS} & 0 \\ 0 & 0 & 0 & 0 & 0 & c_k^{ST} \end{pmatrix} \quad (9)$$

The yield surface is expressed as:

$$\Phi = \bar{\sigma} - R(p) \quad (10)$$

where $R(p)$ corresponds to the flow stress expressed as a function of the accumulated plastic strain p . $R(p)$ is expressed:

$$R(p) = R_0 + Q_1(1 - e^{-b_1 p}) + Q_2(1 - e^{-b_2 p}) \quad (11)$$

Parameter R_0 is set to the normalised yielding stress in rolling direction (L) for each material. Q_1, b_1, Q_2 and b_2 are 4 parameters that mainly control hardening. Plastic anisotropy is only controlled by 12 components in \mathbf{L}_k (4 parameters $c_{1,2}^{LS}, c_{1,2}^{ST}$ are set as 1). a and α_1 influence the shape of yield surface.

2.3.2 Strategy for parameter identification and model prediction

The identification of the various material parameters including 5 hardening parameters and 10 anisotropic parameters was performed using different experimental data. Macro uniaxial-tension (UT) tests in L, T and D loadings, notched-tension (NT2) tests in L, T loadings and micro shear-only (SO) test in L loading were chosen to calibrate hardening and the anisotropy model. The identified model is used to predict the micro tension-only (TO) and two non-proportional loadings 'shear to tension' (ST) as well as 'tension to shear' (TS) in comparison with experimental results.

Step I – optimization of macro UT tests: For the optimization of the computation time, single element calculations were carried out to calibrate with uniaxial-tension (UT) tests. Young's modulus E was set as 74 GPa and the Poisson's ratio was set to 0.3. First, the plastic hardening parameters (R_0, Q_1, b_1, Q_2 and b_2), the anisotropic parameters (12 components c_i^k in \mathbf{L}_k) and yield surface parameter a (α_1 was set to 0.5), under uniaxial-tension state along L, T and D directions were adjusted. Ranges of permitted parameter values were chosen. Besides, 4 parameters $c_{1,2}^{LS}, c_{1,2}^{ST}$ are set to 1 as the yield function is optimized for thin sheets. The nominal stress F/S_0 and width reduction $\Delta W/W_0$ versus engineering strain $\Delta L/L_0$ in loading direction are chosen to calibrate the parameters on experimental results.

Step II – optimization of macro NT2 and micro SO tests: This step aimed at optimizing parameters to fit plasticity for different stress states and higher levels of strain: higher stress triaxiality of notched-tension (NT2) and nearly zero stress triaxiality of shear-only (SO) tests. To achieve this aim, two 3D calculations simulations were added to the optimization to calibrate the parameters on experimental results. Starting from the parameters obtained from step I, all parameters are calibrated again with comparison between nominal stress F/S_0 and notch opening displacement (NOD) for NT2, shear stretch U_{12} for SO. In addition, these tests allow to identify the material hardening at more elevated strain levels.

Step III – prediction on micro TO and non-proportional tests: The parameters obtained from step II are applied to predict the other loading conditions on micro specimens including tension-only (TO) and particularly non-proportional loadings: 'shear to tension' (ST) and 'tension to shear' (TS). These predictions using optimized parameters are compared with experimental results in terms of nominal stress F/S_0 versus shear stretch U_{12} or tension stretch U_{11} .

3 Results

3.1 Mechanical testing results

3.1.1 Vickers hardness test results

The hardness of the 2 mm thick sheets (2198T₃R and 2198T₈R) was identified by an automatic hardness tester HZ₃₀₋₄ (Presi). The force (0.1 kgf) with Vickers indenter was applied along two different lines through the sheet thickness (S). The testing points were distributed along two columns with 50 μm distance to avoid the effect of previous indent as illustrated in Fig.5 (b). The vickers hardness (Hv) profile along the thickness direction is shown in Fig.5 (a). Artificially aged alloy 2198T₈R exhibited a higher hardness (average 164 Hv) than naturally ageing alloy 2198T₃R (average 119 Hv). For each alloy, an obvious hardness reduction of 10% near the middle thickness of raw sheets was found.

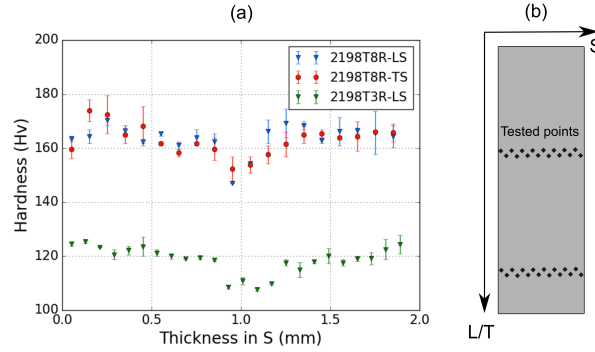


Figure 5: Micro hardness test: (a) Vicker's hardness profiles of average value through the thickness direction and (b) Position of the testing points along two lines.

3.1.2 Proportional loading experiments

Proportional loading results including those of macro specimens of (a) uniaxial-tension (UT) in L,T,D directions, (b) notched-tension (NT₂) in L,T directions as well as micro specimens of (c) shear-only (SO) in L direction and (d) tension-only (TO) in T direction are presented in Fig.6 for 2198T₃R and Fig.7 for 2198T₈R respectively.

2198T₃R: Fig.6 (a) shows the experimental curves in terms of the nominal stress F/S_0 and width reduction ΔW as a function of engineering strain $\Delta L/L_0$ for macro UT tests in L, T and D directions. The curve of nominal stress versus notch opening displacement (NOD) is exhibited in (b) for macro NT₂ specimens in L and T directions. The maximum nominal stress of macro UT and NT₂ reached 382 MPa and 402 MPa, respectively. A moderate plastic anisotropy is found for this alloy. The width reduction was indeed about -0.3 times the longitudinal strain and thereby different from the value for the isotropic case which would be -0.5 , as indicated in form of a dotted line in Fig.6 (a). The yield stress in L-loading is slightly higher, which can be explained by the pre-straining in rolling direction (L) during manufacturing. The nominal stress versus shear stretch of micro specimens SO and tension stretch of TO are presented in Fig.6 (c)(d) respectively. The maximum stress levels of SO and TO are 260 MPa and 394 MPa. Repeated testing results are shown for the small samples to investigate repeatability in terms of plasticity and stretch to fracture. The scatter in shear stretch to fracture U_{12}^{SO} was low and ranged from 0.124 to 0.125 and the tension stretch to fracture U_{11}^{TO} varied from 1.180 to 1.195. The grey zone indicates the scatter range from minimum to maximum found values.

2198T₈R: The tests for artificially aged alloy 2198T₈R in the same layout as Fig.6 are shown in Fig.7. The maximum nominal stress level of macro specimens UT is 497 MPa and NT₂ is 540 MPa. 2198T₈R exhibits a higher stress level but less ductility than naturally aged alloy 2198T₃R. The same moderate plasticity anisotropy is seen as well. The width reduction was also about -0.3 times the longitudinal strain. For micro specimens of 2198T₈R in Fig.7 (c)(d), the maximum nominal stress of SO and TO are 322 MPa and 512 MPa respectively. The shear stretch to fracture scatter of SO (U_{12}^{SO}) was low and ranged from 0.132 to 0.137 and the tension stretch to fracture of TO (U_{11}^{TO}) ranged from 1.105 to 1.130 shown by the scatter bar (grey) for repeated testing. For the TO test an increased scatter in ductility was found compared to the T₃ condition. This might be linked to the higher stress levels that might lead to a stronger sensitivity to microstructure governed damage nucleation. As the samples are small, they may or not contain numerous particle clusters or weak grain boundaries (Rousselier et al. 2017), which may make them prone to the influence of statistics and may have an effect on the macroscopic ductility scatter.

Between two heat treatments of the alloy T₃R and T₈R, obvious ductility reductions were seen in macro UT ($(\Delta L/L_0)_{T3R}^f = 0.16$ versus $(\Delta L/L_0)_{T8R}^f = 0.08$), NT₂ ($NOD_{T3R}^f = 1.0$ versus $NOD_{T8R}^f = 0.5$) experiment

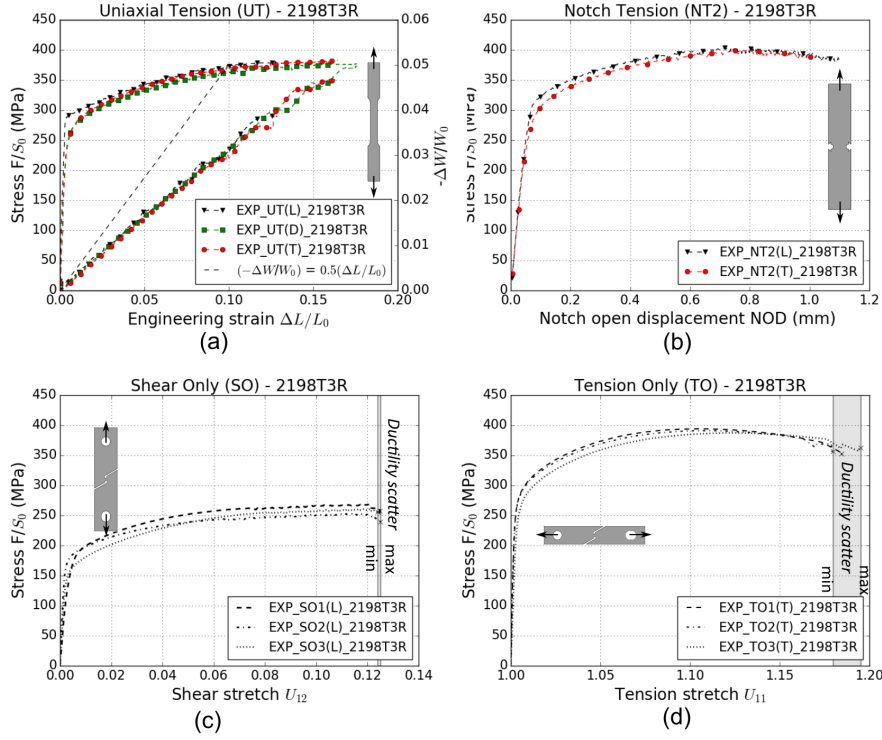


Figure 6: 2198T3R proportional loading experimental results: (a) uniaxial-tension (UT), (b) notched-tension (NT2), (c) shear-only (SO) and (d) tension-only (TO). In a) and b), three symbols represent three loading orientations respectively. Repeated testing results are shown for SO and TO samples.

as well as the micro TO ($U_{11}^{f-T3R} = 1.19$ versus $U_{11}^{f-T8R} = 1.12$) experiment. The artificially aged alloy T8R presents a higher stress level than natural ageing one T3R, which probably is one of the causes of the ductility reduction. Interestingly, the ductility of micro SO test remains close and even stretch to fracture of T3R ($U_{12}^{f-T3R} = 1.124$) is less than that of T8R ($U_{12}^{f-T8R} = 1.135$). The fact that the ductility in shear was so similar between the two heat treatment conditions could be explained by the shear sample geometry that is designed to localize strain in a shear band from the beginning of the test onward. This is different compared to the larger, more homogeneous plastic zone of other sample geometries that may benefit from hardening in the T3 condition and lead to bigger plastic zones and associated macroscopic ductility in T3 condition. Another reason for the similar ductility in T3 and T8 condition in shear could be the relatively low stress levels achieved in shear compared to tensile stress states that may lead to less damage nucleation (Petit et al. 2019).

The macroscopic material behaviour is summarized for both heat treatment conditions in table 3 in terms of yield stress, UTS, engineering strain at the end of uniform elongation and Lankford coefficient. The Lankford coefficient is defined as ratio of the true thickness strain over the true sample width strain: $L_k = \epsilon_{width} / \epsilon_{thickness}$. The thickness strain was obtained by the assumption of incompressibility.

	2198T3R					2198T8R				
	YS	UTS	YS/UTS	UE	L_k	YS	UTS	YS/UTS	UE	L_k
L	290	389	0.745	18.0	0.49	476	504	0.944	7.3	0.48
T	258	386	0.668	18.3	0.50	441	497	0.887	8.7	0.50
D	257	380	0.676	22.1	0.52	435	490	0.888	9.0	0.52

Table 3: Room temperature tensile properties of tested materials (2198T3R and 2198T8R) along L, T and D directions. (YS: yield strength for 0.2% plastic strain (MPa), UTS: ultimate tensile strength (MPa), UE: uniform elongation (%), L_k : Lankford coefficient for a plastic deformation of 5%.

3.1.3 Non proportional tests

Two different types of non-proportional load path change tests on micro cross specimens were performed by loading, unloading and turning the sample by 90°: shear loading in L direction followed by tension loading in T called ‘shear to tension’ (ST) test and tension loading in T followed by shear loading in L called ‘tension to shear’ (TS) tests are presented in Fig.8 for 2198T3R and Fig.9 for 2198T8R respectively.

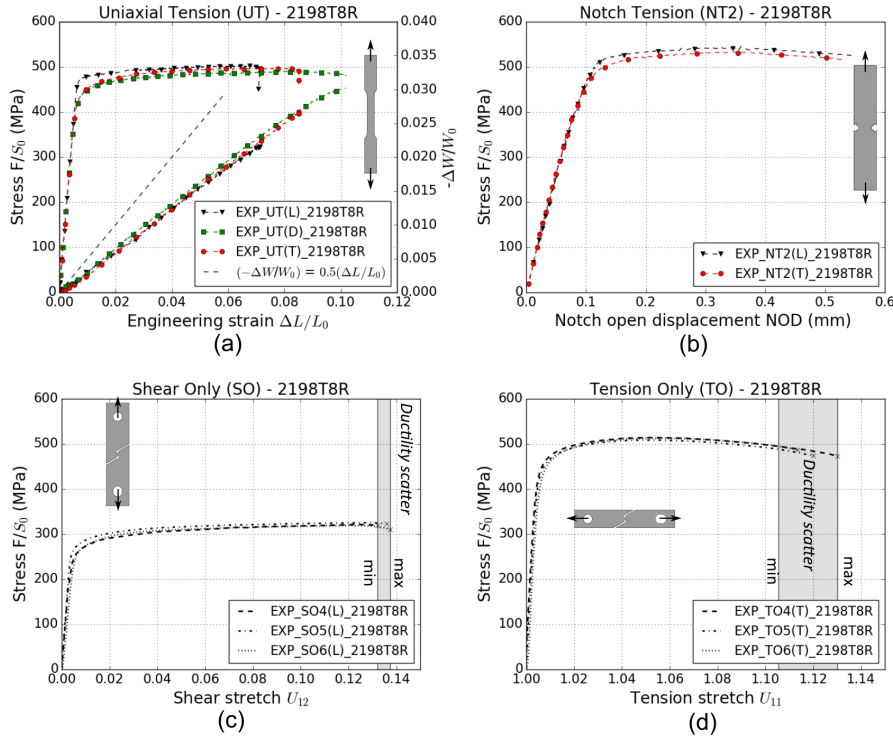


Figure 7: 2198T8R proportional loading experimental results: (a) uniaxial-tension (UT), (b) notched-tension (NT₂), (c) shear-only (SO) and (d) tension-only (TO). Here three different symbols represent three loading orientations respectively. Repeated testing results are shown for SO and TO samples.

2198T₃R: The curves in terms of nominal stress versus (a) shear stretch U_{12} and (b) tension stretch U_{11} from two loading periods of ‘shear to tension’ (ST) are presented in Fig.8. The cross specimen was loaded to around $U_{12} = 0.06$, which was half of monotonic SO shear stretch to fracture ($U_{12} = 0.124$). Subsequently, it was unloaded before applying tension loading till fracture. The 4 initial points were tracked to measure stretch via an optical extensometer during different loading paths, see section 2.2.3. The shear part of the ST-test showed a similar curve as the monotonic SO test that is also plotted for comparison. The nominal stress of tension after shear reached 450 MPa, and the stress at yielding is higher than for the proportional test due to the hardening during the shear loading. In addition, the tension stretch U_{11} started with an initial shift of 0.025 on the tension curve as there was a slight tension stretch during shear loading. The tension stretch to fracture of the ‘shear to tension’ tests ranged from 1.122 to 1.143 with an average value $U_{11}^{ST} = 1.130$, which was reduced by 30% compared to the average stretch to fracture value of TO tests $U_{11}^{TO} = 1.185$. This reduction would be even higher if the initial tension stretch shift during shear loading was not taken into account. The curves of the ‘tension to shear’ (TS) load path change are shown in Fig.8 (c) and (d). The specimen was loaded in tension first till $U_{11} = 1.11$ then unloaded, and it was loaded in shear till fracture. The nominal stress versus tension stretch U_{11} and shear stretch U_{12} are shown in (c)(d) respectively. During the tension period in (c), the stress level of non proportional load TS was very repeatable compared to the proportional TO dashed curve in black. The specimens were unloaded at near maximum stress level around 400 MPa. When the samples were turned and loaded in shear, see (d), the stress level decreased to 220 MPa mainly due to thickness reduction effect during tension loading. The initial offset of shear stretch is due to the shear stretch induced during tension loading. This is mainly due to the fact that the two notches are not aligned. A large scatter zone (blue) of shear stretch to fracture U_{12}^{TS} was found and ranged from 0.100 to 0.126, whose maximum value was close to the monotonic SO shear stretch to fracture U_{12}^{SO} scatter. The average value of stretch to fracture in shear was reduced by about 10% compared to the average stretch to fracture value for the monotonic test. The pre-tension test thereby seems less detrimental than the pre-shear test.

2198T₈R: The same two types of non proportional loadings are presented in Fig.9 for for 2198T₈R. (a) Shear period and (b) tension period of stress – stretch curves for ‘shear to tension’ (ST) are shown. The specimens were loaded in shear loading in L to $U_{12} = 0.06 - 0.08$ for repeated tests and then unloaded. Tension loading in T was applied again till failure. Maximum stress levels reached 600 MPa on tension loading after shear loading, which is higher than that of monotonic TO test (512MPa). The strain to fracture of ST varied from 1.084 to 1.105 while the scatter of TO ranged from 1.105 to 1.130. The average value of stretch to fracture for the ST test was 1.098, which represents a reduction of around 16% compared

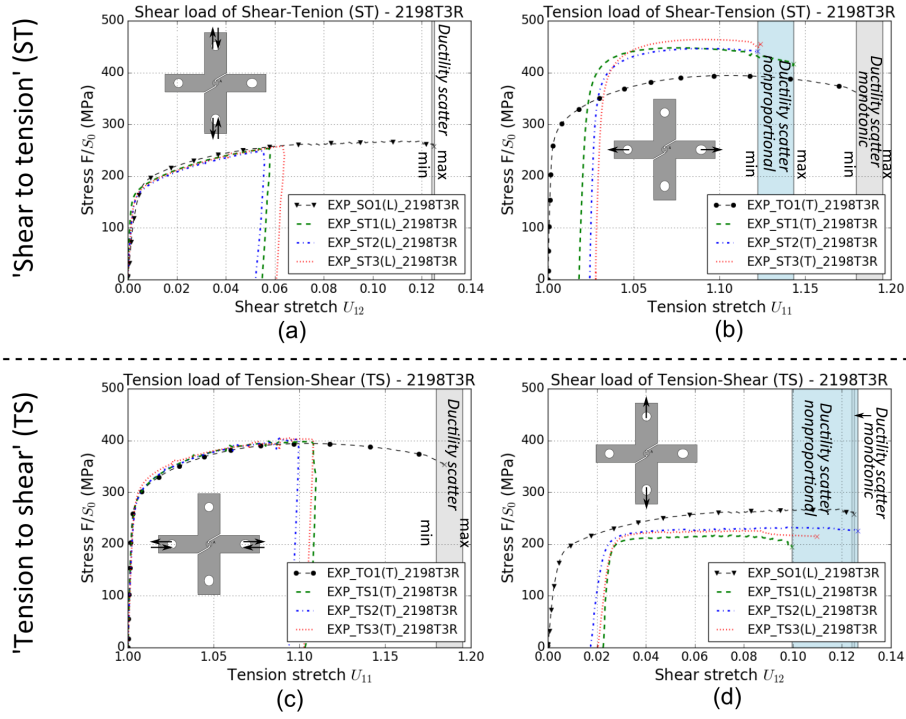


Figure 8: 2198T₃R non-proportional loading experimental results: (a) shear period and (b) tension period of ‘shear to tension’ (ST) loadings, (c) tension period and (d) shear period of ‘tension to shear’ (TS) loadings.

to the average value of stretch to fracture for TO (1.117). Here if the tension stretch shift in pre-shear loading was neglected, the reduction would be even higher.

The results of the ‘tension to shear’ load path change (TS) are shown in Fig.9 (c)(d). The specimens were loaded in tension in T direction to $U_{12} = 1.05 - 1.06$, which is about one half of the fracture stretch under monotonic tensile loading (TO). They were unloaded and then loaded in shear in L direction. The maximum stress levels of shear loading after tension were 300 MPa, which slightly decreased compared to the monotonic SO group. This stress reduction mainly resulted from the thickness reduction effect (cross section reduction) due to pre-tension loading. The strain to fracture scatter (blue) of TS U_{12}^{TS} was large and ranged from 0.117 to 0.157, see Fig.9 (d). The average shear stretch to fracture value of the TS load path change was similar to the average value of shear stretch to fracture of the monotonic test, but the scatter of the shear stretch to fracture of the load path change was a lot stronger than for the monotonic test. The origins of scatter in ductility will be discussed in more detail in the discussion section 4.2 using fields obtained by DIC and fractography.

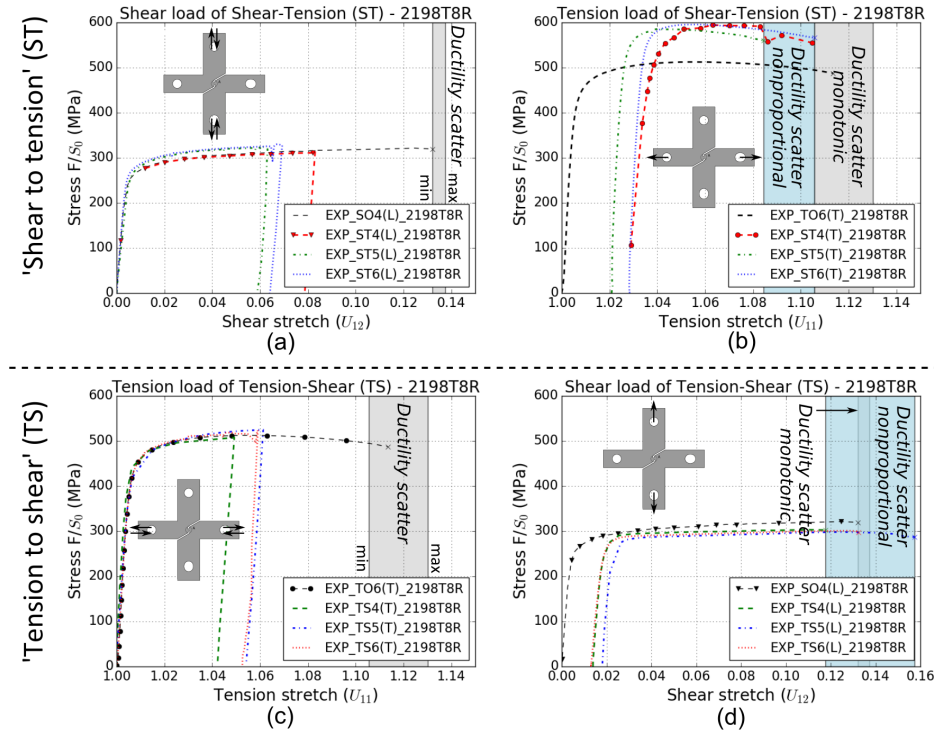


Figure 9: 2198T8R non-proportional loading experimental results: (a) shear period and (b) tension period of ‘shear to tension’ (ST) loadings, (c) tension period and (d) shear period of ‘tension to shear’ (TS) loadings.

The shear and tension stretch to fracture under different loading paths are gathered in table 4 for both materials.

	Proportional U_{11}^{TO}	Non-proportional U_{11}^{ST}	Proportional U_{12}^{SO}	Non-proportional U_{12}^{TS}
2198T ₃ R	1.180-1.195	1.122-1.143	0.124-0.125	0.100-0.126
2198T ₈ R	1.105-1.130	1.084-1.105	0.132-0.135	0.117-0.157

Table 4: Stretch to fracture under different proportional and non proportional loading conditions for the micro specimens of both materials.

3.1.4 Fracture paths and surfaces under different loading conditions

Macroscopic fracture features include the fracture path and fracture surface. The macroscopic fracture path can be identified as flat path or slant path through the sample thickness while the fracture surface can be regarded as rough surface or smooth surface. The fracture paths under different loading conditions will be shown in the following for both 2198T₃R and 2198T₈R. The corresponding results for last strain field before fracture measured by DIC are also given. Microscopically, different types of features are observed on the fracture surfaces. They can be divided into four main types: i) large dimples with sizes larger than 10 μm that are initiated at the coarse precipitates, ii) sub-micrometer dimples that are initiated at dispersoid particles down to nanometer scale, iii) typical shear feature void sheeting that consists of a cluster of sub-micrometer dimples and iv) flat regions without voids. The fractography of four loading conditions TO, ST, SO and TS at various magnifications are exhibited in Fig.11, Fig.12, Fig.13 and Fig.14 respectively obtained by scanning electron microscopy (SEM). Two detectors are utilized: secondary electron (SE₂) and backscattered (HDBSD). The first focus on the fracture shape and more precise relative positions while the latter distinguishes the different phases (i.e. matrix and particle). The applied detector is noted as its abbreviation in the signal A of each image.

2198T₃R: Fig.10 shows the accumulated equivalent strain field at the last step both obtained by the 3D FE simulations and also by surface DIC. The final fracture path of broken micro specimens for four different loadings of the alloy is also given. There is a good agreement between simulations and DIC measurement in terms of the shape of the localized region and also its magnitude. The shapes of the notches are also well reproduced. It can be seen in Figs (a) and (e) that some shear strain is induced during proportional tension loading. Two tension fracture paths of 2198T₃R are seen in Fig.10 (b) tension-only (TO) and (d) ‘shear to tension’ (ST). The proportional loading failed with a flat crack through the thickness. However in the sheet plane (L-T plane) the crack had an angle of 110° and superposed well with the strain

field before failure. In contrast, the crack was slant through the thickness for the ST sample as can be seen in Fig.12 (a). In other words, there is a clear change in fracture plane due to pre-shear. The accumulated equivalent strain level reached only less than 0.45 for both tension fracture groups, but it should be noted that the maximum strain typically occurs at middle thickness of specimen, as known from FE simulations.

The shear fracture planes of 2198T₃R are exhibited in Fig.10 for (f) shear-only (SO) and (h) ‘tension to shear’ (TS). The fracture paths were oriented parallel to shear loads and located at the maximum strain regions for both shear loading conditions in (e) SO and (g) TS. The strain field of the SO test was highly localized up to a magnitude of 0.8 while the field of TS has a wider shear band with maximum value as 0.6 due to the deformed notch from tension preloading. As FE results showed, the strain field of proportional loading SO slightly varied along the thickness direction but the maximum strain region of the non-proportional loading TS is situated in the middle plane due to the pre-tension straining. Fig.13 (a) and Fig.14 (a) show the smoother shear fracture surfaces than tension fractures.

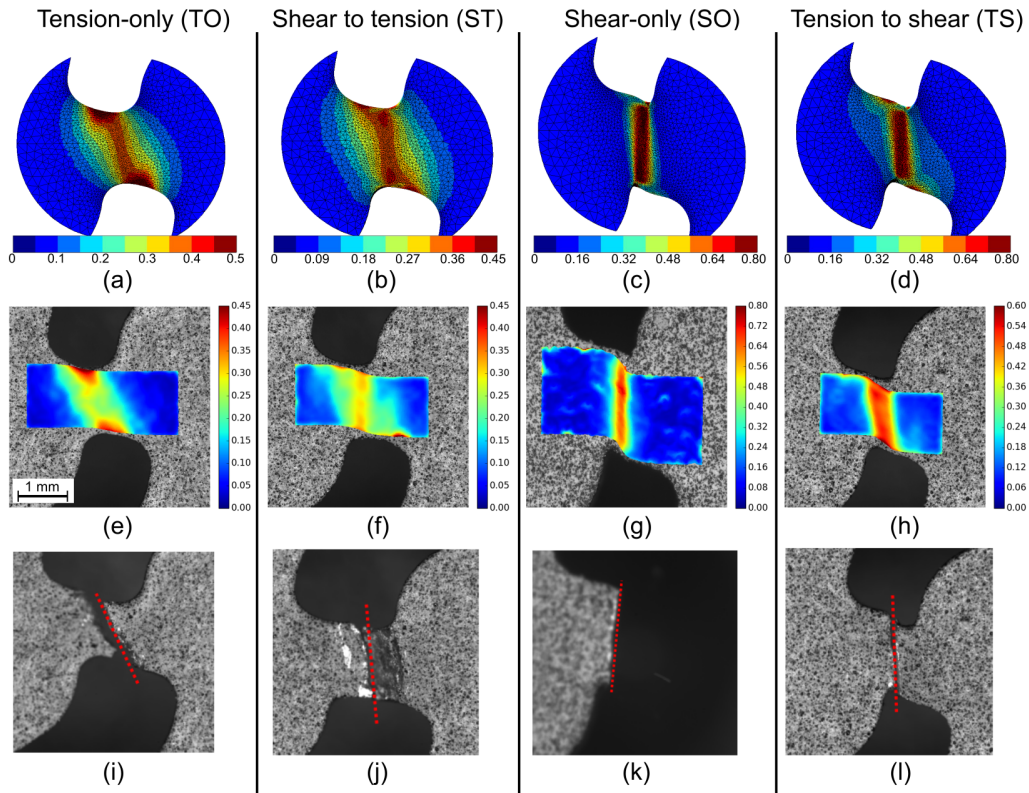


Figure 10: 2198T₃R: (a-d) accumulated equivalent strain on the surface before fracture obtained by 3D FE simulations (e-h) accumulated equivalent strain fields from DIC at last step before fracture and (i-l) Fracture path of proportional tension-only (TO), non-proportional ‘shear to tension’ (ST), proportional shear-only (SO) and non-proportional ‘tension to shear’ (TS) loadings.

Fig.11 (b) exhibits the macroscopic rough fracture surface for the proportional loading TO. Large dimples of size up to 20 μm are shown in (c), which are linked to the intermetallic particles. Broken particles and particle decohesions from the matrix are also found. Locally sub-micrometer dimple features are observed as well in (d). Fig.12 presents the SEM images of non-proportional loading ST. A relatively smooth surface and grain-shaped steps are shown in Fig.12 (a). On the microscopic scale, the steps of grain-shaped features are shown at higher magnification in (c)(d), and these could correspond to the cracks during the pre-shear loading. Some dimples with medium size 1 μm are found and part of them is considered to be initiated on the grain boundaries.

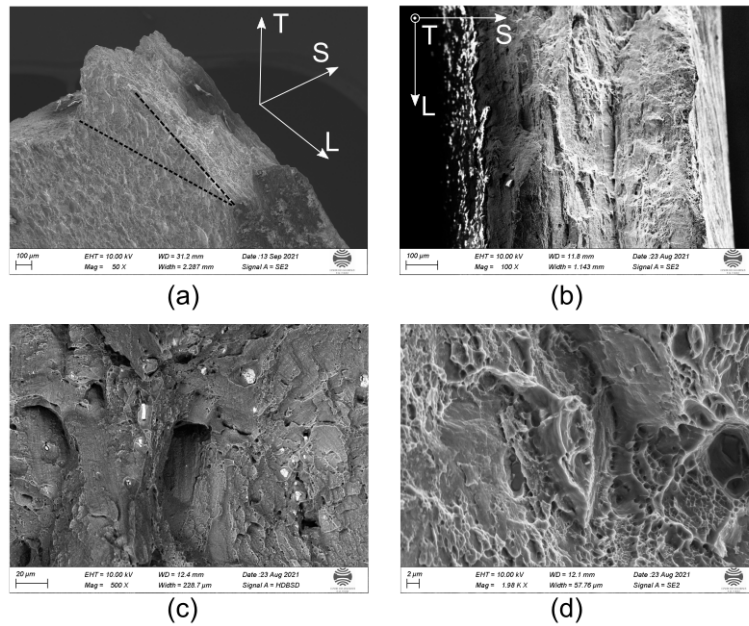


Figure 11: Fractography via scanning electron microscopy (SEM) of 2198T3R under tension-only (TO): (a)(b) Macroscopic rough fracture surface with (c) large dimple that initiated to the intermetallic particles and (d) medium dimples with size down to 2 μm , some of which probably initiated to the grain boundaries.

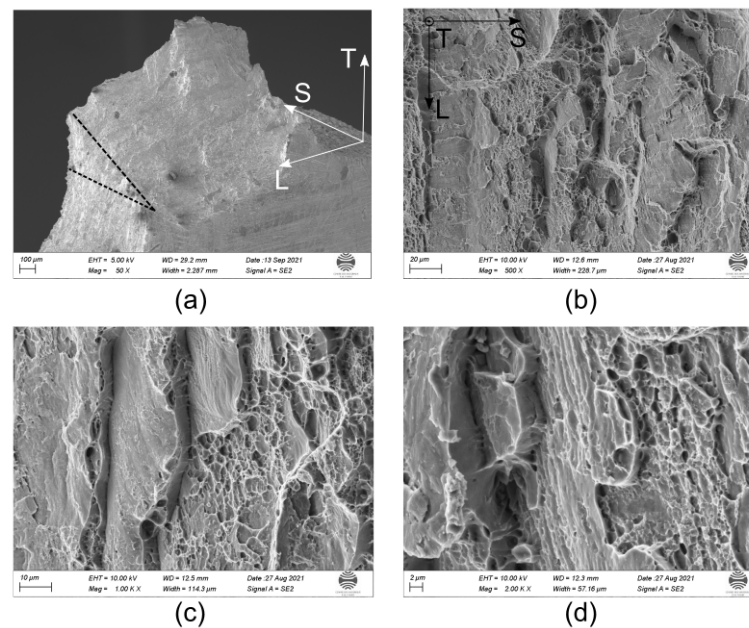


Figure 12: Fractography via scanning electron microscopy (SEM) of 2198T3R under 'shear to tension' (ST): (a) Macroscopic slant fracture path in T-S plane and relative smooth fracture surface, microscopic fracture features like (b) large dimples and (c)(d) grain-shaped steps with medium dimples.

SEM fracture surface images of two loadings that end with shear are shown in Fig.13 of shear-only (SO) and Fig.14 of 'tension to shear' (TS). Both fracture surfaces under proportional SO and non-proportional TS are macroscopically smooth. On the microscopic scale, the elongated dimple cluster is oriented normal to the loading direction in Fig.13 (d). The presence of dispersoids, supposedly Al_3Zr (Nayan et al. 2019), less than 100 nm in diameter are probably the initiation sites of these ductile dimples. For the non-proportional group TS, a flat crack-like feature of 100 μm in length is observed at mid-thickness and it is suspected as the damage from tension pre-loading in Fig.14 (b). The rest area of the fracture surface is more close to the shear damage mechanism as proportional SO loading with void sheeting. Some intermetallic particles are elongated and decohered as shown in (c)(d).

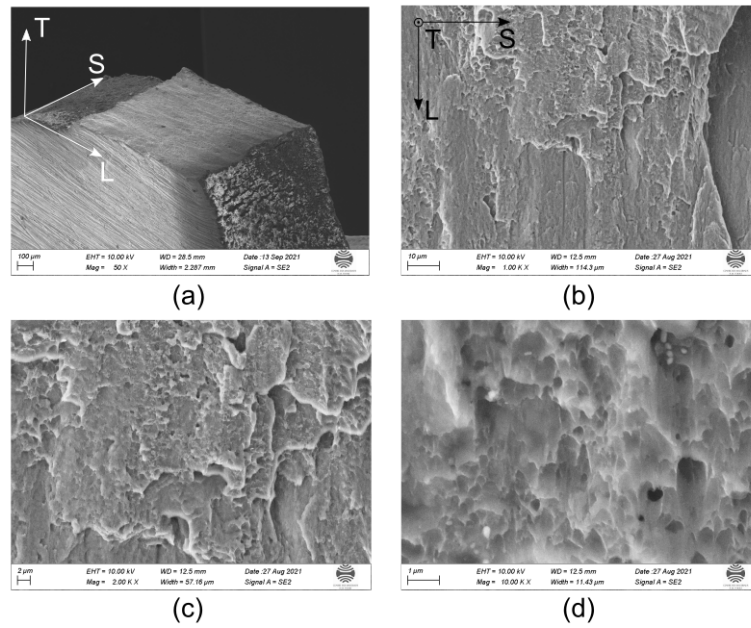


Figure 13: Fractography via scanning electron microscopy (SEM) of 2198T₃R under shear-only (SO): (a) Macroscopic smooth fracture surface, (b)(c) Flat fracture surface and (d) Elongated ductile dimple cluster that initiated on the dispersoids.

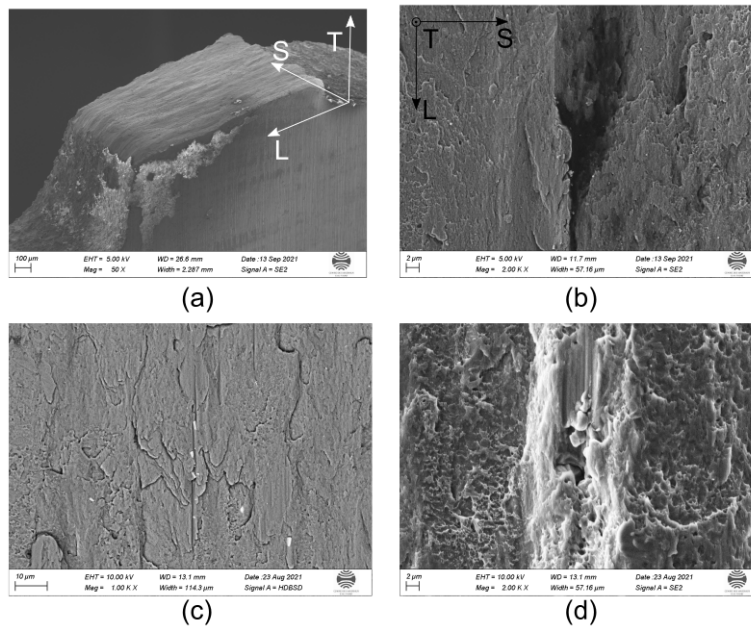


Figure 14: Fractography via scanning electron microscopy (SEM) of 2198T₃R under ‘tension to shear’ (TS): (a) Macroscopic smooth fracture surface, (b) A flat crack-like feature is observed near middle thickness plane, (c) Intermetallic particles are elongated, broken and decohered, (d) Deformed intermetallic particles, medium dimples features including the void sheeting shear feature.

2198T₈R: The same layout of accumulated equivalent strain field of last step before fracture and fracture path of 2198T₈R are presented in Fig.15. Fracture paths match well with their maximum strain locations as 2198T₃R. Similar to the global tension stretch reduction, the local strain level on surface of 2198T₈R shows lower strain values as well than the material in T₃R condition. It showed a lower strain value around 0.40 compared to 0.45 of 2198T₃R in TO. For shear dominated cracks shear-only (SO) and ‘tension to shear’ (TS), the cracks are oriented parallel to the loading direction as shown in T₃R. For the sake of brevity, the fractography of 2198T₈R result is given in A.2. Conclusions are similar to those of T₃R condition.

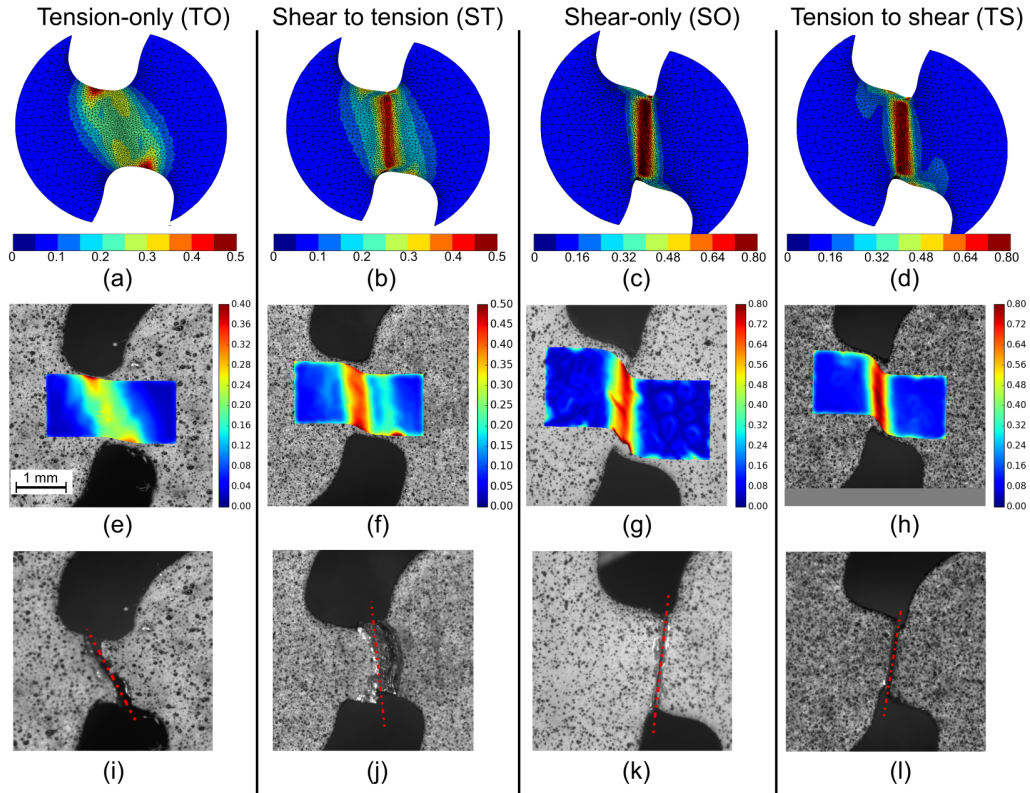


Figure 15: 2198T8R: (a-d) Accumulated equivalent strain on the surface before fracture obtained by 3D FE simulations, (e-h) Accumulated equivalent strain fields from DIC at last step before fracture, (i-l) Fracture path of proportional tension-only (TO), non-proportional ‘shear to tension’ (ST), proportional shear-only (SO) and non-proportional ‘tension to shear’ (TS) loadings.

3.2 Identification of material parameters and optimization

Based on the strategy detailed in section 2.3.2, the model accounting for plastic anisotropy was identified by using calibrations with proportional loadings macro uniaxial-tension (UT) in L, T and D directions, notched-tension (NT₂) in L,T tests and micro test shear-only (SO) in L. The 5 optimized hardening parameters are given in table 5 and the 10 anisotropic parameters are shown in table 6 for each material. The fits of numerical simulations using the optimized parameters with experimental results are given in Fig.16 for 2198T₃R and Fig.17 for 2198T₈R.

The macro UT stress-strain curves of experiment (point) and simulations (full line) in three directions were fitted and exhibited in Fig.16 (a). The macro NT₂ stress versus displacement curves in L, T are presented in (b). Plasticity model simulations fit well with experimental results. The micro SO stress – shear stretch curve from simulation agreed well with one representative experimental test in (c) despite a small mismatch near yield point. The width reduction is also well fitted.

The same tests and numerical results as above are shown in Fig.17 for 2198T₈R. There are good agreements in (a) macro UT and (c) micro SO tests between numerical and experimental results. Less than 2% stress difference is found in NT₂ in both L, T directions is found in (c), which is due to the less weight set in macro NT₂ tests than in UT tests during the optimization of plasticity parameters.

Material	R_0	Q_1	b_1	Q_2	b_2
2198T ₃ R	217.2	18.370	578.855	166.561	10.909
2198T ₈ R	450	41.645	749.659	98.278	25.551

Table 5: Optimized parameters for plasticity hardening.

Material	a	α_1	c_1^{TT}	c_1^{LL}	c_1^{SS}	c_1^{TL}	c_1^{LS}	c_1^{ST}
			c_2^{TT}	c_2^{LL}	c_2^{SS}	c_2^{TL}	c_2^{LS}	c_2^{ST}
2198T ₃ R	6.160	0.500	1.084	1.058	0.702	0.901	1	1
			0.767	0.790	0.853	0.712	1	1
2198T ₈ R	15.9	0.500	1.192	1.219	0.867	1.070	1	1
			0.720	0.772	1.343	1.155	1	1

Table 6: Optimized parameters for plasticity anisotropy.

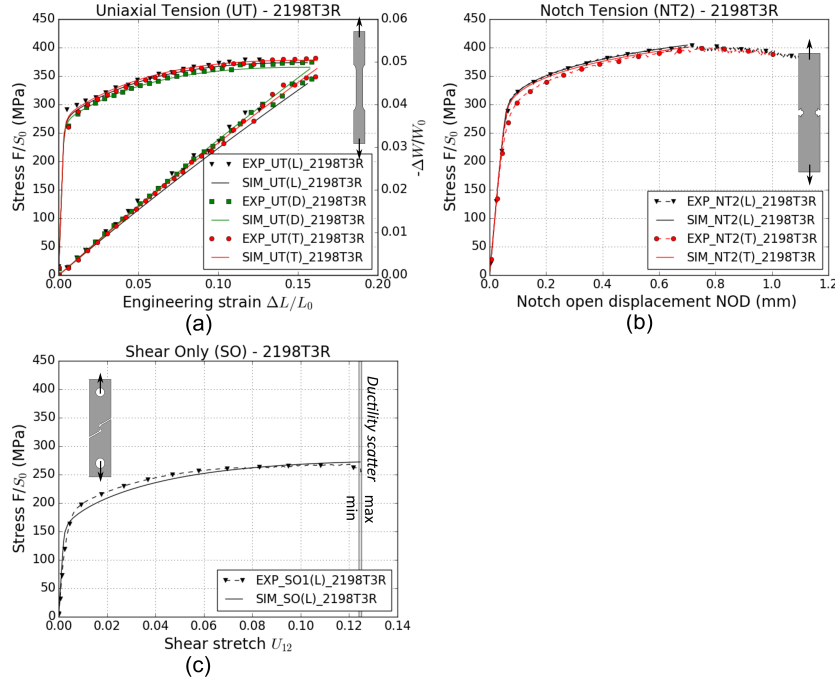


Figure 16: 2198T₃R calibrated FE simulation results (full line) with experimental groups: (a) uniaxial-tension (UT), (b) notched-tension (NT₂), and (c) shear-only (SO).

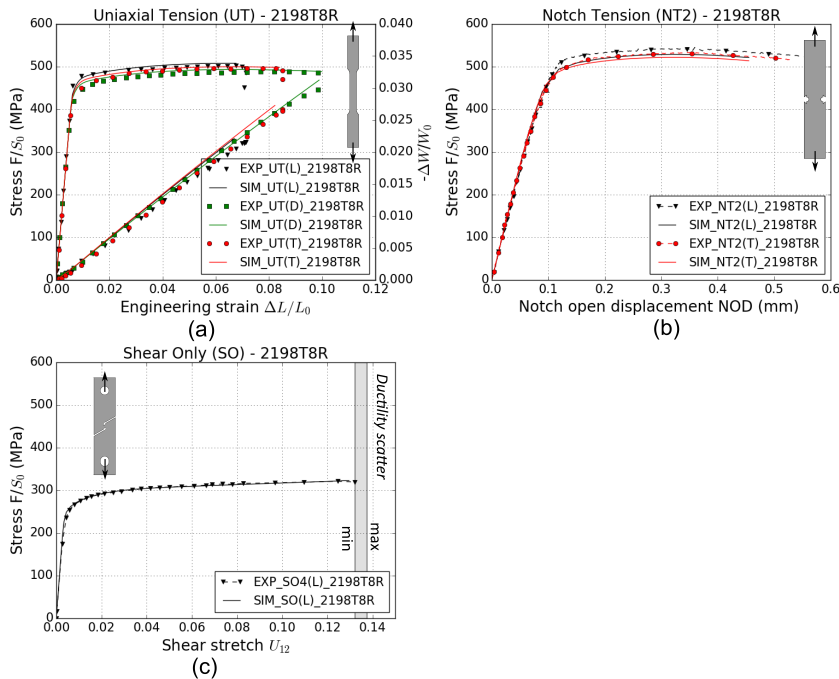


Figure 17: 2198T₈R calibrated FE simulation results (full line) with experimental groups: (a) uniaxial-tension (UT), (b) notched-tension (NT₂) and (c) shear-only (SO).

3.3 Prediction results of tension only and non-proportional loadings

The model with optimized parameters was used to simulate the small specimens under tension-only (TO) and non-proportional loadings including ‘shear to tension’ (ST) and ‘tension to shear’ (TS) to predict and compare with the experimental results in Fig.18 for 2198T₃R and Fig.19 for 2198T₈R.

2198T₃R predictions (full line) not only fit well the TO experimental result (dashed line), but also in both loading periods of non proportional loadings ST and TS in Fig.18. In Fig. 19 (d) the nominal stress drop at the very end of the shear load is not predicted correctly. This can be explained by the fact that some damage development may occur in the experiment at high strains which is not accounted for in the simulation.

On the other hand, a good agreement between predictions and experiments is obtained as well for 2198T₈R in Fig.19 except 2.4% maximum stress over-prediction in micro TO compared to the average experimental data. Consider that the model is identified using macro tension tests (UT and NT₂), experimental result of micro TO can be effected by specimen size. It is believed that the mechanical fields predicted by the 3D FE simulation can be used to interpret future *in situ* testing results in terms of strain, stresses and, in particular, stress triaxiality.

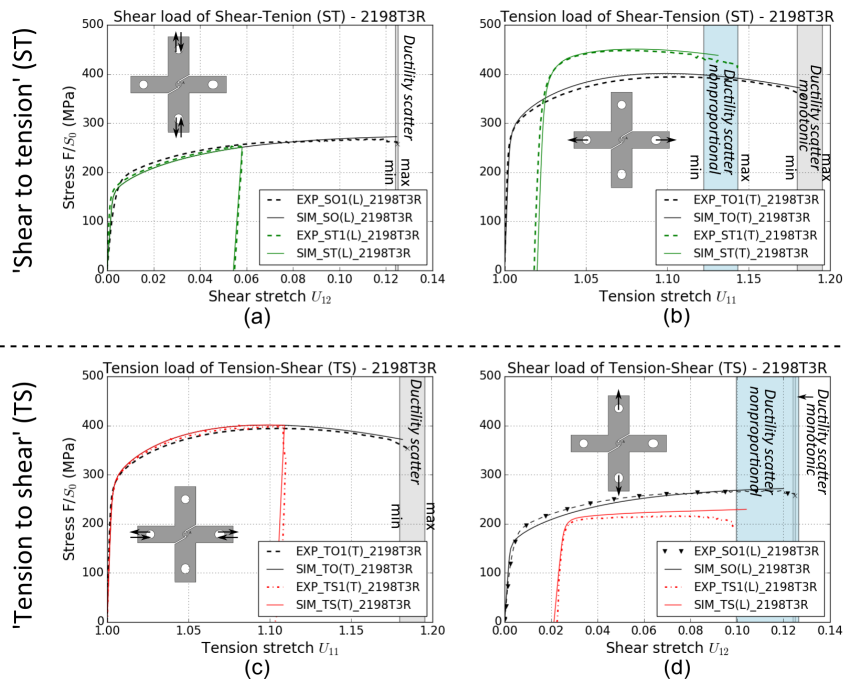


Figure 18: 2198T₃R optimised FE prediction results (full line) with experimental groups: (a) shear period and (b) tension period of ‘shear to tension’ (ST) loadings, (c) tension period and (d) shear period of ‘tension to shear’ (TS) loadings.

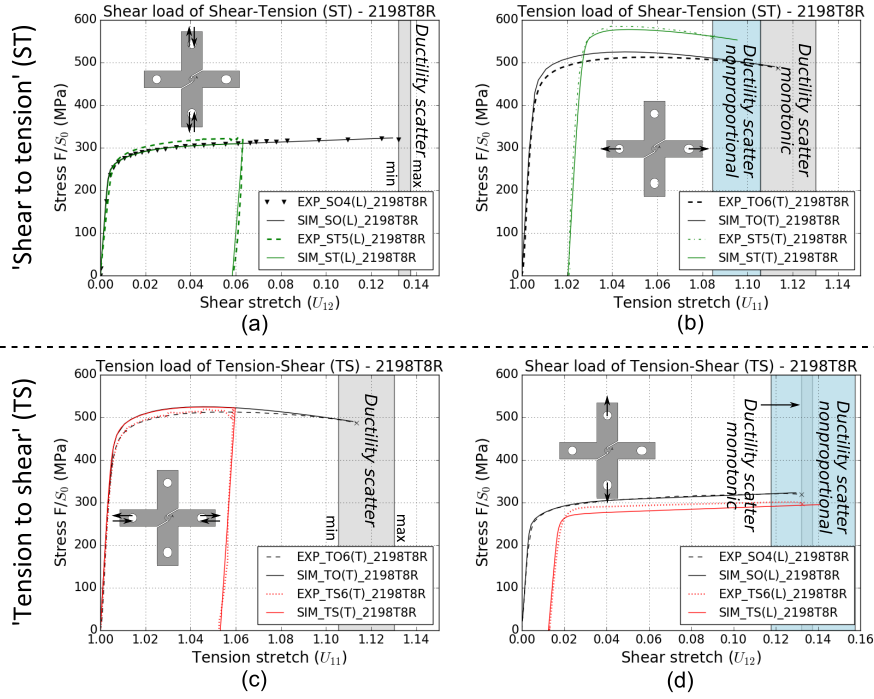


Figure 19: 2198T8R optimized FE prediction results (full line) with experimental groups: (a) shear period and (b) tension period of ‘shear to tension’ (ST) loadings, (c) tension period and (d) shear period of ‘tension to shear’ (TS) loadings.

4 Discussion

4.1 Suitability of the plasticity model for load path change

The constitutive model with Bron-Besson anisotropic yield condition succeeded in predicting the mechanical behaviors of two alloys for non proportional load path change tests. In this model, flow stress only contains the isotropic hardening part not kinematic part although Deschamps et al. 2013 found a Bauschinger tests (tension – compression) for a similar alloy provided as a 6 mm thick sheet. In the present work, shear and tension loadings do not reach the compression yielding point. In addition, the data base lacks compression data to optimize since buckling often occurs for thin sheet specimen under compression. Due to the lack of compression data and due to the fact that at the chosen strain levels no Bauschinger effect was seen, the present model identification is considered as suitable to predict mechanical fields during the load path changes that can then be used to interpret the strain and damage seen in *in situ* laminography tests (Kong et al. 2021).

4.2 Load path change effect on ductility

Compared to proportional loading tension-only (TO) loading, an obvious reduction on ductility is found for non-proportional ‘shear to tension’ (ST) for both materials. The average stretch to fracture of non-proportional ST reduced 29% and 16% for the alloy in T3R and T8R condition respectively compared to the proportional TO test result. Brüning et al. 2021 also found 33% displacement reduction from experimental results between tension-only and shear (45% failure displacement of shear only)-followed-by-tension based on an H-shaped cross sample in aluminium alloy 6082T6. These reductions suggest that pre-shear loading might nucleate damage before tension, which can be identified in *in situ* experiments (Kong et al. 2021). In addition, pre-shear loadings harden the material and lead to a higher yield stress, which also could be the cause of ductility reduction if brittle damage nucleation processes are at play (Petit et al. 2019).

On the other hand, for two loadings that end with shear: shear-only (SO) and ‘tension to shear’ (TS), the reduction varies from 0% to 20% strongly as a function of the extent of pre-tension loading. Two TS tests (TS2, TS3) were chosen to discuss here: TS2 and TS3 were loaded in tension till different levels of tension stretch: $U_{11}^{TS2} = 1.05$ and $U_{11}^{TS3} = 1.06$, see Fig.8 (c), and then they were loaded in shear till failure at $U_{12}^{TS2} = 0.126$ and $U_{12}^{TS3} = 0.109$ in Fig.8 (d). The stress level of TS is lower than that of proportional SO because of the thickness reduction during the pre-tension period. The local accumulated equivalent strain fields on pre-tension end of both tests are shown in Fig.20 (a)(d). The highly strained region of test TS3, that was more loaded in pre-tension than TS2, is larger than that of TS2. It means that the higher pre-loading in tension resulted in more detrimental effect on stretch to fracture. The strain fields show two shear bands with different width at (b) shear end before fracture in Fig.20. The maximum strain

level reached 0.80 on surface of TS₂, whose values (both shear stretch and local strain level) are close to proportional shear-only (SO) test. On the other hand, the test with higher pre-load (TS₃) generated a wider shear band with lower maximum strain around 0.60 on specimen surface. It is suspected that strain is less localized but more widely distributed in shear band due to the deformed geometry of two notches. In pre-tension load in Fig.8 (c), the TS₂ was loaded to the maximum stress while the TS₃ was loaded after maximum stress point. The force drop in the latter TS₃ is likely to be linked to the necking effect. Brünig et al. 2021 found a strong scatter as well (from 0% to 47%) for ‘tension to shear’ load path change experiments using a H-shaped cross sample. This ductility reduction sensitively relies on the applied pre-tension extent and the subsequent local thickness reduction effect.

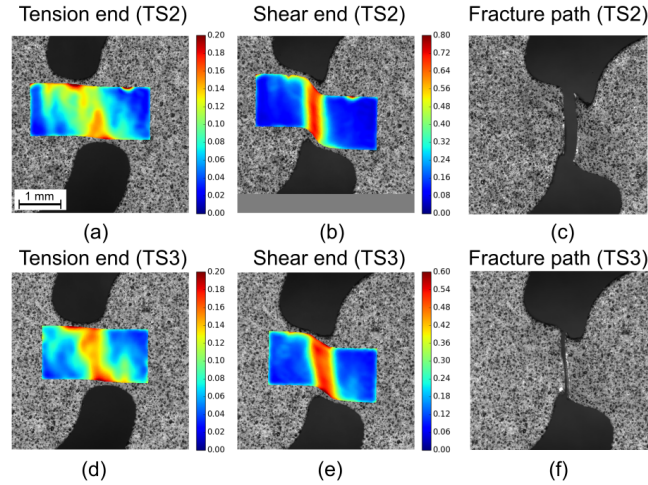


Figure 20: 2198T₃R accumulated equivalent strain fields of (a)(d) tension end and (b)(e) shear end periods from two tension-followed-by-tension (TS) tests TS₂, TS₃ and their (c)(f) fracture paths.

4.3 Specimen size effect

In this study, the model with optimized parameters using the macro-test dataset succeeded in predicting the experimental results of micro 1 mm thickness samples except micro TO of 2198T₈R with 2.4% maximal stress over-prediction. In order to discuss this conclusion, a 2× magnified tension-only (TO) specimen with 2 mm thickness was manufactured and tested. The stress level of macro TO specimen coincided with the numerical prediction shown in Fig.21. The numerical simulations give a same stress – stretch curves for both dimensions. The slight stress drop could be explained by the limited number of grains in the ligament or by lower hardness in the middle plane for micro TO sample. On the other hand, the strain to fracture of macro TO was well within the range of micro TO ductility scatter. The identification is proved to be specimen size independent. Gorji et al. 2021 compared specimens with a size ratio of 20:1 with thickness 2 mm and 100 μm, and they found that the plasticity obtained from micro experiments matched those obtained from conventional macro experiments whereas the ductility was slightly reduced in micro experiments. They declared the differences are small within the range of uncertainty and concluded that the model identified on micro-experiments validates the results of conventional macro-experiments.

5 Conclusion

The microstructure of the material was characterized in terms of grain size, texture and particle as well as void volume fraction.

Concerning the **mechanical testing** of the material in T₃ and T₈ heat treatment conditions, the following conclusions can be drawn:

- Uniaxial tensile tests were performed on the full thickness (2 mm) samples in L, T and diagonal directions and in L and T directions for notched tensile samples.
- The material in both heat treatment conditions showed a moderate anisotropy, particularly in the width reduction during tensile testing.
- A small 1 mm thick cross shaped sample was designed to be able to perform ‘shear to tension’ or ‘tension to shear’ load path changes in a 3D *in situ* imaging environment for another study (Kong et al. 2021). The loading was first performed in one direction followed by unloading and rotation of the sample by 90° and reloading up to fracture.
- A four point optical extensometer based on DIC was defined to measure stretch in tension and shear. The aim was to be unaffected of any rigid body rotations and to synchronize the experiment with 3D finite element simulations.

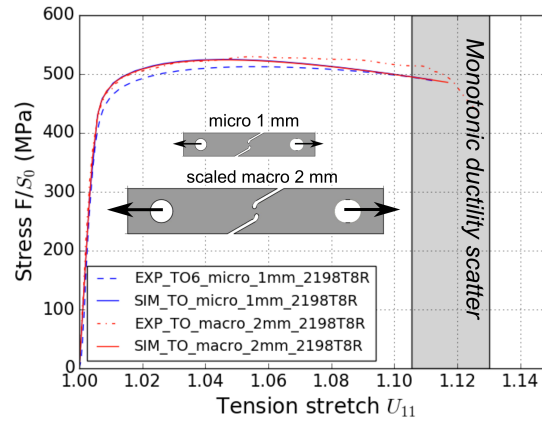


Figure 21: The nominal stress - tension stretch curves of tension only (TO) specimens with scaled macro 2 mm thickness and micro 1 mm thickness.

- Shear, tension as well as ‘shear to tension’ and ‘tension to shear’ experiments were carried out using the small samples.
- As expected, the yield strength of the T8 condition was about twice the one of the T3 condition. The ductility during tensile testing and notched tensile testing was about half for the T8 condition compared to the T3 condition. Interestingly, the shear-stretch to fracture measured during shear experiments was very similar for both materials.
- The ‘shear to tension’ load path change led to a reduction of tension stretch at fracture of 29% and 16% for T3 and T8 respectively.
- The ‘tension to shear’ load patch change did not lead to a significant reduction in shear stretch to fracture but increased substantially the scatter in shear stretch to fracture for both heat treatment conditions.
- The fracture plane of the ‘shear to tension’ load path change sample was slant though the sample thickness and the crack was straight in the sample plane, indicating the pre-shear affected the failure mode as it was different from the one of the TO sample.
- Fractography revealed micrometre sized dimples for the tension loading, grain related flat zones and very small shear dimples linked to dispersoid particles under shear loading.

Concerning the **simulations** using the anisotropic finite element model and isotropic hardening, the conclusions are:

- The model was fitted using data obtained on the uniaxial tensile and notched tensile samples loaded in different directions as well as the small shear sample. A good fit is obtained in terms of stress strain curves as well as in terms of width strains for the uniaxial tension samples.
- The load patch changes are predicted using the model with identified parameters. A good prediction of the stress-stretch curves was achieved and it is assumed that the predicted mechanical fields give a good estimate of the reality.

The damage development during load patch changes should be investigated in more detail by 3D imaging to identify the role of damage on ductility reduction during the load path changes (Kong et al. 2021).

Acknowledgements

ANR (Lambda project:ANR17-CE08-0051 and Alicandte project) is gratefully acknowledged for its financial support. The European Synchrotron Radiation Facility (ESRF) beamline ID19 is thanked for providing beamtime (experiment ma4333). We thank Constellium for materials supply.

6 Bibliography

- Abedini, A., C. Butcher, and M. Worswick (2018). "Experimental fracture characterisation of an anisotropic magnesium alloy sheet in proportional and non-proportional loading conditions". *International Journal of Solids and Structures* 144-145, pp. 1–19
- Al Akhrass, D., J. Bruchon, S. Drapier, and S. Fayolle (2014). "Integrating a logarithmic-strain based hyperelastic formulation into a three-field mixed finite element formulation to deal with incompressibility in finite-strain elastoplasticity". *Finite Elements in Analysis and Design* 86, pp. 61–70
- Bai, Y. and T. Wierzbicki (2008). "A new model of metal plasticity and fracture with pressure and Lode dependence". *International Journal of Plasticity* 24.6, pp. 1071–1096. DOI: <https://doi.org/10.1016/j.ijplas.2007.09.004>
- Bao, Y. and T. Wierzbicki (2004). "On fracture locus in the equivalent strain and stress triaxiality space". *International Journal of Mechanical Sciences* 46.1, pp. 81–98. DOI: <https://doi.org/10.1016/j.ijmecsci.2004.02.006>
- Barlat, F., D. J. Lege, and J. C. Brem (1991). "A six-component yield function for anisotropic materials". *International Journal of Plasticity* 7.7, pp. 693–712. DOI: [https://doi.org/10.1016/0749-6419\(91\)90052-Z](https://doi.org/10.1016/0749-6419(91)90052-Z)
- Belytschko, T., W. Liu, and B. Moran (2000). *Nonlinear Finite Elements for Continua and Structures*. English. John Wiley Sons, Ltd
- Besson, J. and R. Foerch (1997). "Large scale object-oriented finite element code design". *Computer Methods in Applied Mechanics and Engineering* 142.1, pp. 165–187
- Bron, F. and J. Besson (2004). "A yield function for anisotropic materials Application to aluminum alloys". *International Journal of Plasticity* 20.4, pp. 937–963
- Brüning, M., O. Chyra, D. Albrecht, L. Driemeier, and M. Alves (2008). "A ductile damage criterion at various stress triaxialities". *International Journal of Plasticity* 24.10. Special Issue in Honor of Jean-Louis Chaboche, pp. 1731–1755. DOI: <https://doi.org/10.1016/j.ijplas.2007.12.001>
- Brüning, M., M. Zistl, and S. Gerke (2021). "Numerical Analysis of Experiments on Damage and Fracture Behavior of Differently Preloaded Aluminum Alloy Specimens". *Metals* 11.3
- Butcher, C. and A. Abedini (2017). "Shear confusion: Identification of the appropriate equivalent strain in simple shear using the logarithmic strain measure". *International Journal of Mechanical Sciences* 134, pp. 273–283
- Chen, J. (Apr. 2011). "**Ductile tearing of AA2198 aluminium-lithium sheets for aeronautic application**". Theses. École Nationale Supérieure des Mines de Paris
- Chen, J., Y. Madi, T. F. Morgeneyer, and J. Besson (2011). "Plastic flow and ductile rupture of a 2198 Al–Cu–Li aluminum alloy". *Computational Materials Science* 50.4. Proceedings of the 19th International Workshop on Computational Mechanics of Materials, pp. 1365–1371. DOI: <https://doi.org/10.1016/j.commatsci.2010.06.029>
- Deschamps, A., B. Decreus, F. De Geuser, T. Dorin, and M. Weyland (2013). "The influence of precipitation on plastic deformation of Al–Cu–Li alloys". *Acta Materialia* 61.11, pp. 4010–4021. DOI: <https://doi.org/10.1016/j.actamat.2013.03.015>
- Ehrström, J.-C. and T. Warner (May 2000). "Metallurgical Design of Alloys for Aerospace Structures". *Aluminium Alloys - Their Physical and Mechanical Properties*. Vol. 331. Materials Science Forum. Trans Tech Publications Ltd, pp. 5–16. DOI: [10.4028/www.scientific.net/MSF.331-337.5](https://doi.org/10.4028/www.scientific.net/MSF.331-337.5)
- Gerke, S., M. Zistl, A. Bhardwaj, and M. Brüning (2019). "Experiments with the Xo-specimen on the effect of non-proportional loading paths on damage and fracture mechanisms in aluminum alloys". *International Journal of Solids and Structures* 163, pp. 157–169. DOI: <https://doi.org/10.1016/j.ijsolstr.2019.01.007>
- Gorji, M. B., J. Furmanski, and D. Mohr (2021). "From macro- to micro-experiments: Specimen-size independent identification of plasticity and fracture properties". *International Journal of Mechanical Sciences* 199, p. 106389. DOI: <https://doi.org/10.1016/j.ijmecsci.2021.106389>
- Gross, A. J. and K. Ravi-Chandar (2016). "On the deformation and failure of Al 6061-T6 at low triaxiality evaluated through in situ microscopy". *International Journal of Fracture* 200, pp. 185–208. DOI: <https://doi.org/10.1007/s10704-016-0078-x>
- Helfen, L., T. Baumbach, P. Mikulík, D. Kiel, P. Pernot, P. Cloetens, and J. Baruchel (2005). "High-resolution three-dimensional imaging of flat objects by synchrotron-radiation computed laminography". *Applied Physics Letters* 86.7, p. 071915
- Helfen, L., T. F. Morgeneyer, F. Xu, M. Mavrogordato, I. Sinclair, B. Schillinger, and T. Baumbach (2012). "Synchrotron and neutron laminography for three-dimensional imaging of devices and flat material specimens". *International Journal of Materials Research* 2, pp. 170–173
- Hill, R. (1950). *The mathematical theory of plasticity*. Oxford university press
- Karafilis, A. and M. Boyce (1993). "A general anisotropic yield criterion using bounds and a transformation weighting tensor". *Journal of the Mechanics and Physics of Solids* 41.12, pp. 1859–1886. DOI: [https://doi.org/10.1016/0022-5096\(93\)90073-O](https://doi.org/10.1016/0022-5096(93)90073-O)

- Kong, X., L. Helfen, M. Hurst, D. Hanschke, D. Missoum-Benziane, J. Besson, T. Baumbach, and T. F. Morgeneyer (2021). “3D *in situ* study of damage during a ‘shear to tension’ load path change in an aluminium alloy”. *Under preparation*
- Le-Jolu, T., T. F. Morgeneyer, and A. F. Gourgues-Lorenzon (2010). “Effect of joint line remnant on fatigue lifetime of friction stir welded Al–Cu–Li alloy”. *Science and Technology of Welding and Joining* 15.8, pp. 694–698
- Lemaitre, J. and J.-L. Chaboche (1990). *Mechanics of Solid Materials*. Cambridge University Press. DOI: [10.1017/CBO9781139167970](https://doi.org/10.1017/CBO9781139167970)
- Madi, Y., Y. Shinohara, and J. Besson (2020). “Effect of prestrain on ductility and toughness in a high-strength line pipe steel”. *International Journal of Fracture* 224.1, pp. 15–29
- Morgeneyer, T. F., J. Besson, H. Proudhon, M. Starink, and I. Sinclair (2009). “Experimental and numerical analysis of toughness anisotropy in AA2139 Al-alloy sheet”. *Acta Materialia* 57, pp. 3902–3915
- Morgeneyer, T. F., M. Khadyko, A. Buljac, L. Helfen, F. Hild, A. Benallal, T. Børvik, and O. S. Hopperstad (2021). “On crystallographic aspects of heterogeneous plastic flow during ductile tearing: 3D measurements and crystal plasticity simulations for AA7075-T651”. *International Journal of Plasticity* 144, p. 103028. DOI: <https://doi.org/10.1016/j.ijplas.2021.103028>
- Nayan, N., S. V. S. N. Murty, R. Sarkar, A. K. Mukhopadhyay, S. Ahlawat, S. K. Sarkar, M. J. N. V. Prasad, and I. Samajdar (2019). “The Anisotropy of Serrated Flow Behavior of Al-Cu-Li (AA2198) Alloy”. *Metallurgical and Materials Transactions A* 50, pp. 5066–5078
- Onaka, S. (2010). “Equivalent strain in simple shear deformation described by using the Hencky strain”. *Philosophical Magazine Letters* 90.9, pp. 633–639
- Onaka, S. (2012). “Comment on “A comparison of the von Mises and Hencky equivalent strains for use in simple shear experiments””. *Philosophical Magazine* 92.18, pp. 2264–2271
- Papasidero, J., V. Doquet, and D. Mohr (2015). “Ductile fracture of aluminum 2024-T351 under proportional and non-proportional multi-axial loading: Bao–Wierzbicki results revisited”. *International Journal of Solids and Structures* 69–70, pp. 459–474. DOI: <https://doi.org/10.1016/j.ijsolstr.2015.05.006>
- Petit, T., J. Besson, C. Ritter, K. Colas, L. Helfen, and T. F. Morgeneyer (2019). “Effect of hardening on toughness captured by stress-based damage nucleation in 6061 aluminum alloy”. *Acta Materialia* 180, pp. 349–365
- Pineau, A., A. Benzerga, and T. Pardoen (2016). “Failure of metals I: Brittle and ductile fracture”. *Acta Materialia* 107, pp. 424–483
- Roth, C. C. and D. Mohr (2018a). “Determining the strain to fracture for simple shear for a wide range of sheet metals”. *International Journal of Mechanical Sciences* 149, pp. 224–240
- Roth, C. C., T. F. Morgeneyer, Y. Cheng, L. Helfen, and D. Mohr (2018b). “Ductile damage mechanism under shear-dominated loading: In-situ tomography experiments on dual phase steel and localization analysis”. *International Journal of Plasticity* 109, pp. 169–192
- Rousselier, G., T. Morgeneyer, S. Ren, M. Mazière, and S. Forest (2017). “Interaction of the Portevin–Le Chatelier phenomenon with ductile fracture of a thin aluminum CT specimen: experiments and simulations”. *Int. J. Fract.* 206.1, pp. 95–122
- Tancogne-Dejean, T., C. C. Roth, T. F. Morgeneyer, L. Helfen, and D. Mohr (2021). “Ductile damage of AA2024-T3 under shear loading: Mechanism analysis through in-situ laminography”. *Acta Materialia* 205, p. 116556
- Tarigopula, V., O. Hopperstad, M. Langseth, and A. Clausen (2009). “An evaluation of a combined isotropic-kinematic hardening model for representation of complex strain-path changes in dual-phase steel”. *European Journal of Mechanics - A/Solids* 28.4, pp. 792–805. DOI: <https://doi.org/10.1016/j.euromechsol.2008.12.004>
- Taylor, R. (2000). “A mixed-enhanced formulation for tetrahedral finite elements”. *International Journal for numerical methods in engineering* 47, pp. 205–227
- Warner, T. (July 2006). “Recently-Developed Aluminium Solutions for Aerospace Applications”. *Aluminium Alloys 2006 - ICAA10*. Vol. 519. Materials Science Forum. Trans Tech Publications Ltd, pp. 1271–1278
- Xavier, M. D., N. B. de Lima, R. L. Plaut, and C. G. Schön (2015). “Strain path dependence of the FLC₀ formability parameter in an interstitial free steel”. *The International Journal of Advanced Manufacturing Technology* 80.5, pp. 1077–1085. DOI: [10.1007/s00170-015-7103-5](https://doi.org/10.1007/s00170-015-7103-5)

A Appendices

A.1 Mesh convergence

Mesh convergence study was conducted on shear-only (SO), tension-only (TO) and ‘shear to tension’ (ST) simulations with element size varying from 10 μm to 200 μm . The curves force versus stretch are exhibited in Fig.22 (a)(b)(c)(d). The force error stands for the difference between the actual force and the reference force F_{10} from the fine mesh 10 μm on the chosen points ($U_{12} = 0.08, U_{11} = 1.11$). The force error versus element length is shown in Fig.22 (e). It is concluded that simulations have been converged with the element size down to 50 μm since the error is less than 0.2%.

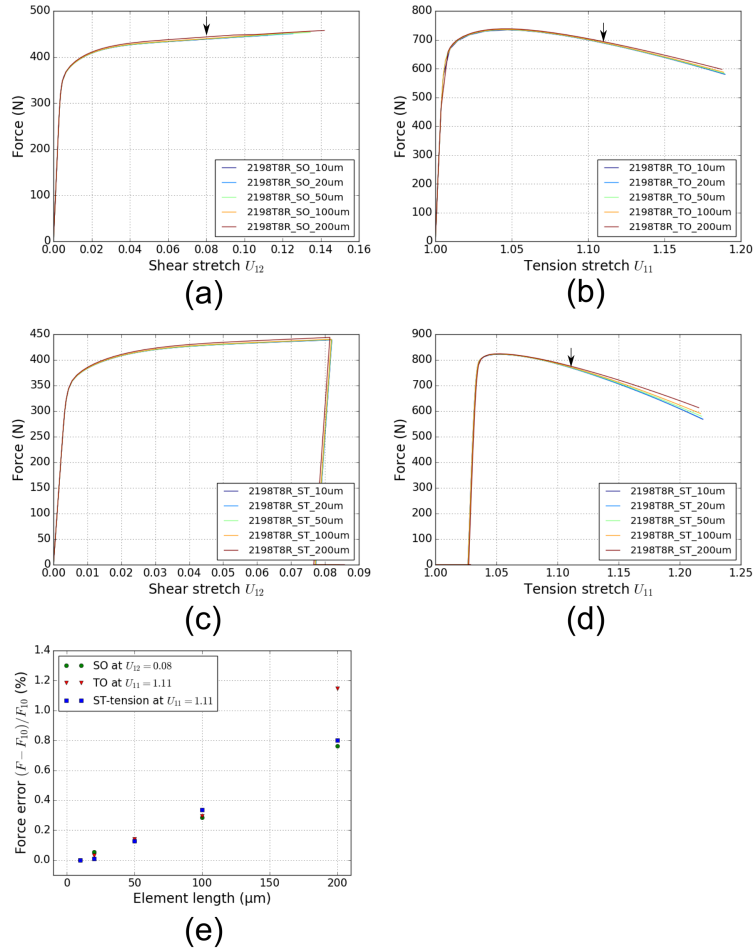


Figure 22: The force versus stretch curves from the simulations of different mesh size from 10 μm to 200 μm under (a) shear-only (SO), (b) tension-only (TO) as well as (c) shear period and (d) tension period of non-proportional ‘shear to tension’ (ST). (e) Mesh convergence in terms of the curve force error versus element length size.

A.2 Fractography of 2198T8R

The fractography of four loading conditions TO, ST, SO and TS at various magnifications are exhibited in Fig.23, Fig.24, Fig.25 and Fig.26 via SEM. The features are similar as described for 2198T₃R in 3.1.4.

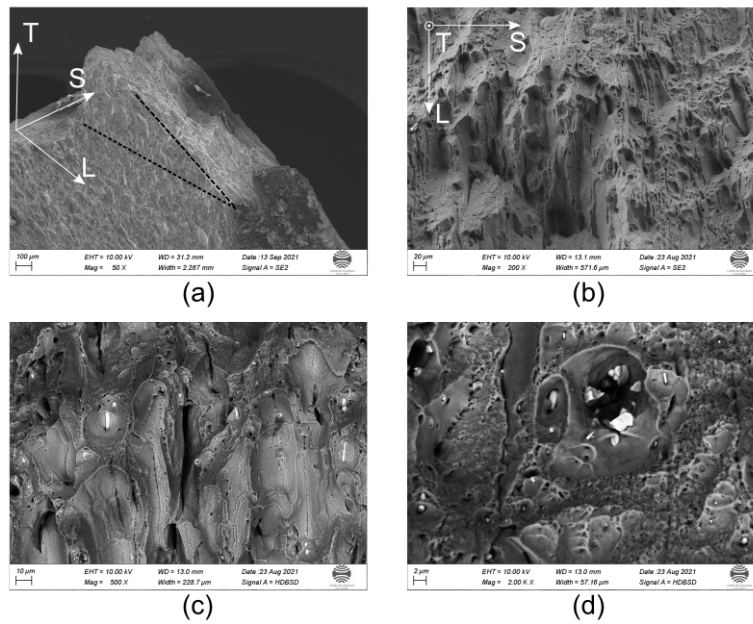


Figure 23: Fractography via scanning electron microscopy (SEM) of 2198T₃R under tension-only (TO): (a)(b) Macroscopic rough fracture surface with (c) large dimple that initiated to the intermetallic particles and (d) medium dimples with broken particles.

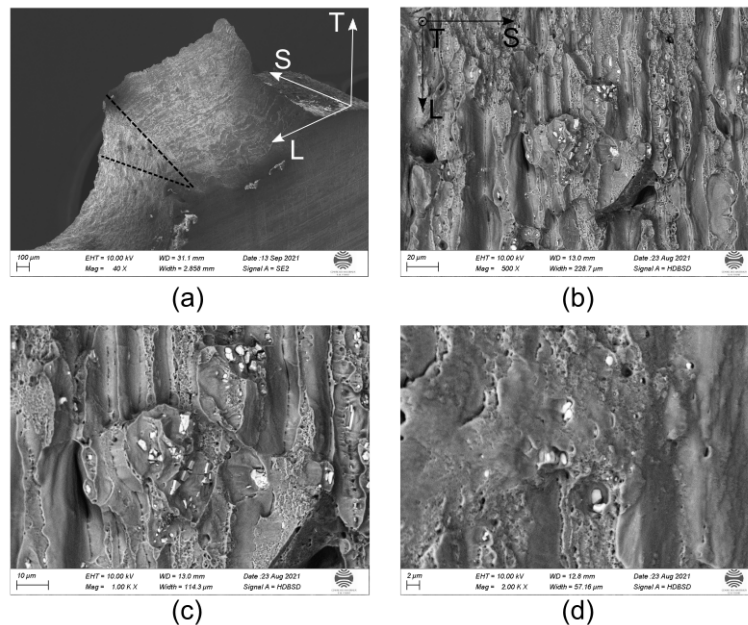


Figure 24: Fractography via scanning electron microscopy (SEM) of 2198T₃R under ‘shear to tension’ (ST): (a) Macroscopic slant fracture path in the T-S plane and relative smooth fracture surface, microscopic features like (b) large dimple that initiated to the (c) intermetallic particles and grain-shaped steps with medium dimples that initiated on the grain boundaries and (d) submicro dimples with the broken intermetallic particles.

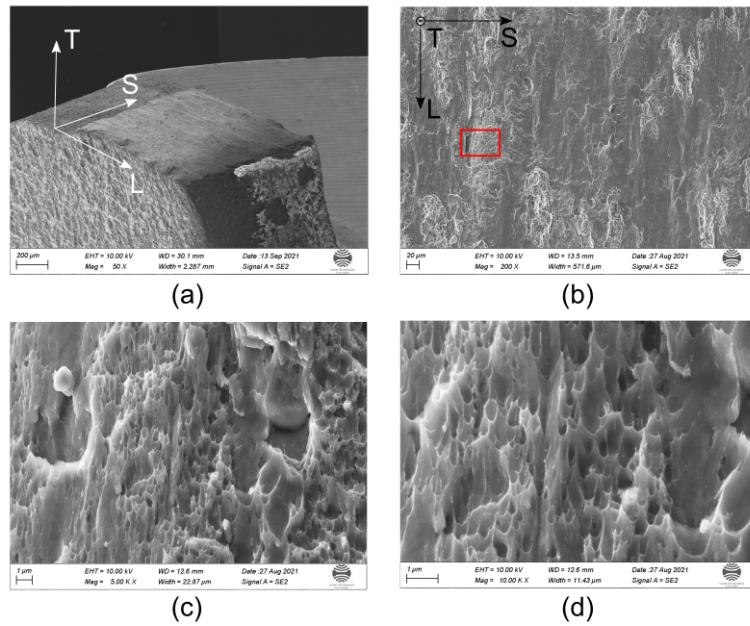


Figure 25: Fractography via scanning electron microscopy (SEM) of 2198T₃R under shear-only (SO): (a) Macroscopic smooth fracture surface, (b)(c) flat fracture surface and (d) Elongated ductile dimple cluster that initiated on the dispersoids.

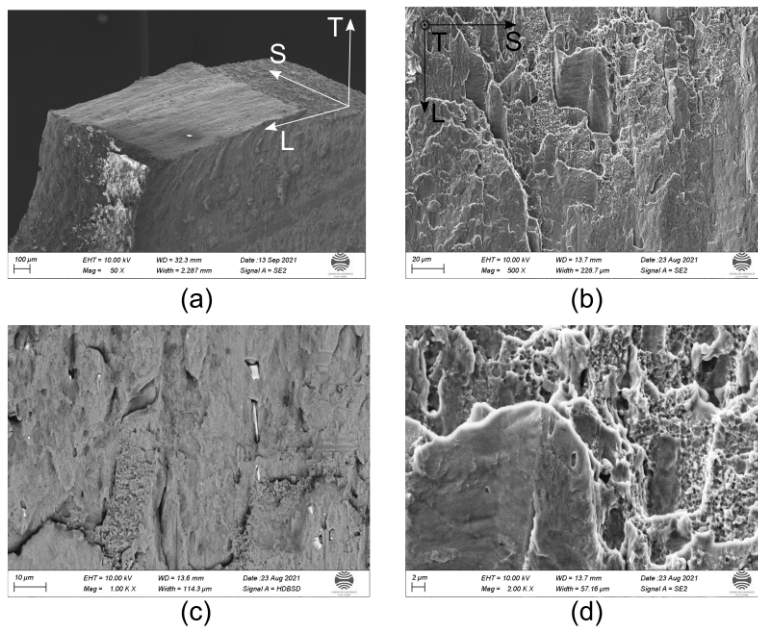


Figure 26: Fractography via scanning electron microscopy (SEM) of 2198T₃R under 'tension to shear' (TS): (a) Macroscopic smooth fracture surface, (b) shear fracture feature, (c) elongated intermetallic particles and (d) flat-like fracture feature with void sheeting features of submicro dimple cluster.